

Report #HT-01-2017

Laser interferometry

D. Naylor

Department of Mechanical & Industrial Engineering

Ryerson University, Toronto

Ontario, Canada

Abstract

An introduction is given to the optical setup and principle of operation of classical and holographic interferometers that are used for convective heat transfer measurements. The equations for the evaluation of the temperature field are derived and methods of analysis are discussed for both two-dimensional and three-dimensional temperature fields. Emphasis is given to techniques for measuring local heat transfer rates. For two-dimensional fields, a method is presented for measuring the surface temperature gradient directly from a finite (wedge) fringe interferogram. This “direct gradient method” is shown to be most useful for the measurement of low convective heat transfer rates. For three-dimensional fields, the equations for calculating the beam-averaged local heat flux are presented. The measurement of the fluid temperature averaged along the light beam is shown to be approximate. However, an analysis is presented showing that for most cases the error associated with temperature variations in the light beam direction is small. Digital image analysis of interferograms to obtain fringe spacings is also discussed briefly.

1 Introduction

Interferometry has been widely used for full-field temperature measurement and for the evaluation of local convective heat transfer rates, with some of the earliest work dating back to the 1930's and 1940's [1, 2]. Until recently, most studies were performed by classical interferometry, using a Mach-Zehnder interferometer or similar instrument. But, in the past ten years, the use of holographic interferometry has become increasingly widespread.

A review of the recent literature shows that both classical [3, 4] and holographic [5, 6, 7] interferometry are currently in wide use. In fact, in recent

years there appears to have been a resurgence of interest in interferometry that has paralleled the rapid developments in heat transfer modeling. Complex numerical models require careful validation by experiment. For a variety of problems, interferometry can provide full-field temperature visualization and detailed local heat transfer data that are ideal for the verification of numerical predictions.

Interferometry, both classical and holographic, has some outstanding advantages compared to many other heat transfer measurement techniques. Perhaps the most significant advantage is that interferometry is non-intrusive, permitting measurements with no disturbance of the temperature or flow field. Another very useful feature is that the optical temperature measurements are free from thermal inertia. So, real-time measurements can be made of high speed transient phenomena.

However, interferometry also has some significant limitations, which must be considered. One obvious requirement is that the test fluid must be transparent to laser light. Also, interferometry requires a clean, low vibration environment and a skilled operator. For this reason its use is almost always restricted to a laboratory setting. In addition, since variations in the refractive index are integrated in the direction of the light beam, interferometry is best suited for making local heat transfer measurements in two-dimensional temperature fields. As will be discussed in Section 4.2, true local measurements in a three-dimensional field require the application of tomographic reconstruction methods.

An examination of the literature reveals that interferometry has been applied primarily to laminar heat transfer problems. Only a few studies have considered turbulent conditions. For example, a study by Lockett et al. [8,9] considered turbulent forced convection on a heated plate. In this investigation, high speed cinematography was used to capture the rapid near-wall temperature fluctuations. Another study, by Khuen and Goldstein [10,11] used a time-averaging method for temperature field visualization in a turbulent free convective flow.

In this chapter, a brief introduction is given to the optical setup and principle of operation of classical and holographic interferometers. The analysis of interferograms is discussed for both two- and three-dimensional temperature fields, with an emphasis on techniques for evaluating local convective heat transfer rates. To conclude, a simple digital image processing system for semi-automating the analysis of interferograms is presented.

2 Classical interferometry

One of the most common instruments used for classical interferometry is the Mach-Zehnder interferometer (MZI). Figure 1 shows a sketch of the optical setup of a typical MZI. The input optics consist of a beam expander and parabolic mirror, which are used to expand the laser into a large diameter collimated beam. At the first beam splitter (half-silvered mirror), the expanded beam is divided into two separate beams of approximately equal intensity, which are initially in phase. As shown in Figure 1, the test beam travels past the heated (or cooled) experimental model and the reference beam travels through the ambient air, which has uniform temperature.

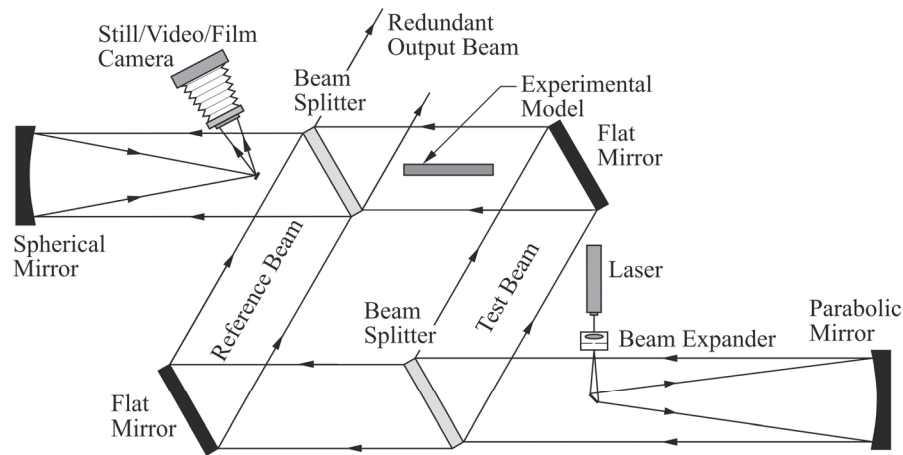


Figure 1: Plan view of the optical setup of a Mach-Zehnder interferometer.

Because of the change in refractive index with temperature of the fluid in the experimental model, the speed of light in the model section is different than in the reference beam. As a result, the test beam undergoes a phase shift relative to the reference beam. Because of the wave properties of light, when the two beams are recombined at the second beam splitter, this phase shift produces constructive and destructive interference in the output beam. This interference pattern can be analyzed to give a real-time measurement of the temperature field in the experimental model, which can be observed and recorded continuously.

For classical interferometry, high precision optical components must be used to obtain an interference fringe field that is free of distortion. In order to accurately measure the phase shift caused by the change in refractive index of the fluid in the test model, all other sources of phase disturbance must be reduced. From the point where the laser beam is split, to the point where the beams are recombined, all wave front distortions caused by the optical components must be kept to a minimum. Typically, this requires that the beam splitters, first-surface mirrors and test section optical windows (if required) be flat to approximately one twentieth of a wavelength of light ($\lambda/20$). Also, the surfaces of the beam splitters and optical windows must be parallel to approximately 1 arc second ($1/3600$ of a degree). For large diameter beams, components with these specifications are very expensive. In addition, if the test section is to be pressurized, Khuen [10] has found that thick optical windows must be used in order to reduce the stress-induced deflection of the window surface. Even slight curvature under loading can cause significant wave front distortions in the test beam, leading to measurement errors.

It should also be noted that for the test and reference beams to interfere, the two light beams must be coherent. This is why lasers are used exclusively for modern interferometry. The narrow spectral bandwidth of gas lasers produces long coherence lengths. As a result, the optical path lengths of the test and reference beams can be substantially different (by many centimeters) and still interfere

strongly. Nevertheless, in practice, care should be taken to make the two path lengths close to the same, in order to get maximum fringe contrast. Further details of the design and operation of classical interferometers can be found in references [12, 13].

When the test beam and reference beam are almost perfectly parallel upon recombination at the second beam splitter, the interferometer is said to be in the “infinite fringe” setting. In this setting, the lines of constructive and destructive interference (called fringes) are lines of constant refractive index for a two-dimensional field. These fringes are also lines of constant density. So, for a gas when the pressure is constant, lines of constant fringe shift correspond to isotherms. An example of an infinite fringe interferogram is shown in Figure 2(a). This interferogram is of a steady free convective boundary layer on a vertical isothermal plate, taken in air with a MZI.

For some applications, the reference and test beams are purposely misaligned by a small angle upon recombination at the second beam splitter. This is called the “finite fringe” or “wedge fringe” setting. To understand the fringe pattern in this case, consider two plane waves diverging by a small angle θ , as illustrated in

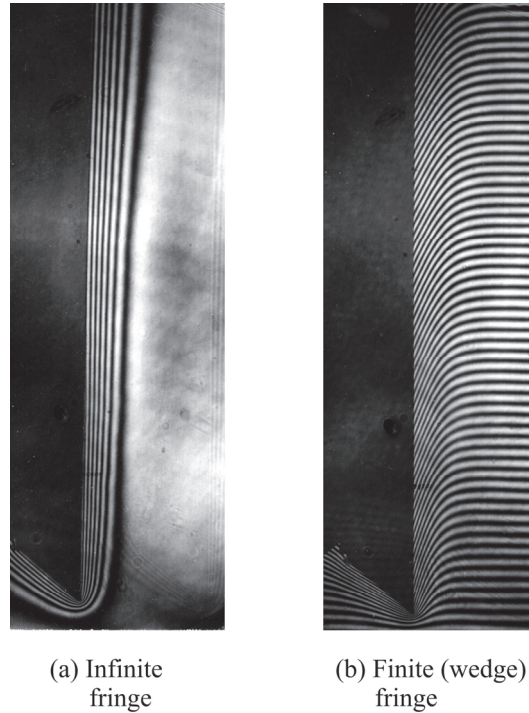


Figure 2: Infinite and finite (wedge) fringe interferograms of laminar free convection from a heated isothermal flat plate in air.

Figure 3. Lines have been drawn through the wave crests of both beams, normal to the direction of light propagation (z), assuming that both waves are plane. It can be seen that constructive interference occurs where the maxima of the two beams coincide. So, the intensity distribution varies across the beams, as indicated in the upper section of the figure. A screen placed perpendicular to the z-axis will display alternate dark and light fringes. From geometry, it is evident that the spacing between fringes is:

$$d = \frac{\lambda/2}{\sin(\theta/2)}, \quad d \approx \frac{\lambda}{\theta} \quad \text{for small } \theta \quad (1)$$

It should be emphasized that the angle of divergence (θ) is shown greatly enlarged in Figure 3. For a finite fringe spacing of $d=2$ mm, with a He-Ne laser ($\lambda= 6.328 \times 10^{-7}$ m), the angle between the test and reference beams is only about $1/50^{\text{th}}$ of a degree. As the angle (θ) approaches zero, the finite fringes get further apart and the distance (d) between the fringes approaches infinity. This is the reason for the term “infinite fringe” setting.

An example of a finite fringe interferogram is shown in Figure 2(b). In this interferogram, the undisturbed horizontal finite fringes in the ambient were produced by slight misalignment of the test and reference beams in the vertical plane. Note that the finite fringes are straight horizontal lines in the ambient, where

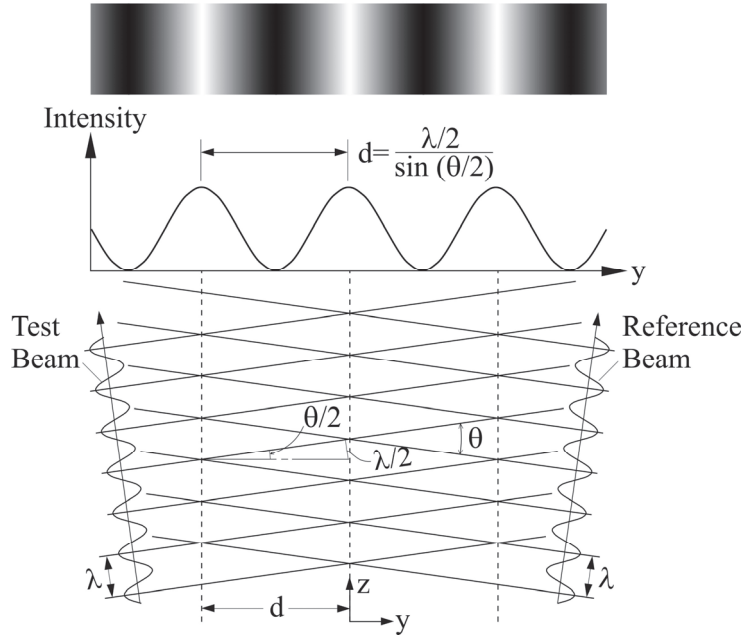


Figure 3: Finite fringe pattern produced by two intersecting plane light waves.

the temperature is uniform. But, the fringes bend as they enter the thermal boundary layer. The fringes bend because the test beam experiences an additional phase shift as it passes near the heated plate and is no longer a plane wave in this region.

Although the finite fringe setting does not provide the clear temperature field visualization of the infinite fringe setting, it does have some advantages. In practice, a finite fringe condition is much easier to achieve than the infinite fringe setting and is less susceptible to vibrations. Also, as will be shown in Section 4.1.1, finite fringes can be used to make measurements in regions of low temperature gradient, where measurements would be difficult using the infinite fringe setting. So, in effect, the finite fringe setting can be used to increase the sensitivity of the interferometer.

Several optical configurations other than the MZI have been used for classical interferometry [14, 15]. One particularly noteworthy configuration is the Twyman-Green interferometer, shown in Figure 4. Note that for this optical setup, the test beam makes a double pass through the experimental model. This results in a doubling of the sensitivity; twice as much phase shift occurs in the test beam for the same fluid temperature difference. So, twice as many interference fringes are produced, compared to a MZI. This configuration can be useful for increasing the

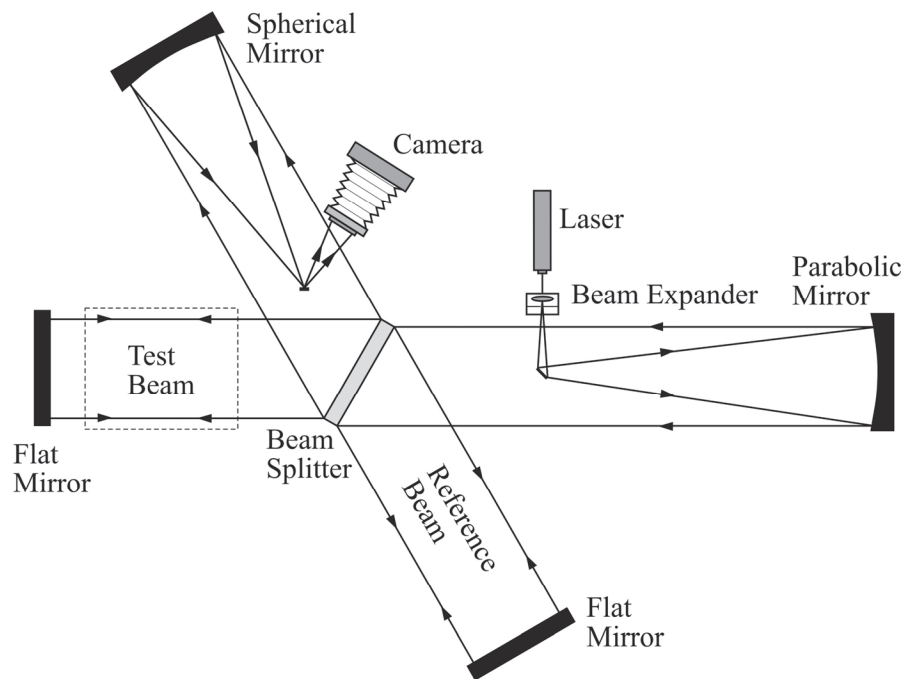


Figure 4: Plan view of the optical setup for a Twyman-Green interferometer.

number of fringes when measurements must be made at a low temperature difference or when the test model must be short in the light beam direction. Papple and Tarasuk [16] have used a Twyman-Green interferometer to study free convection around a vertical cylinder in air. Also, Fröhlich et al. [17] have studied the temperature field in SF₆ using this optical setup. One drawback noted by Papple [18] is that the interferograms tend to be slightly lower in quality (i.e. higher levels of noise) than for the MZI configuration. Also, alignment of the optics is particularly critical since the test beam must travel along the precisely same path in both directions past the experimental model. Other optical configurations that use a multiple-pass of the test beam have also been proposed [19, 20].

3 Holographic interferometry

An overview of the application of holography to the measurement of refractive index fields will be presented in this section. The detailed theory of holography is too involved to discuss here. The reader is referred to the literature [21, 22, 23, 24, 25] for an in-depth explanation and mathematical description.

Figure 5 shows a typical optical setup of a holographic interferometer for convective heat transfer measurements. Clearly, the optical configuration has many similarities to that of a MZI. Comparing Figures 1 and 5 reveals that the main difference between a MZI and a holographic interferometer is that the second beam splitter is replaced with a holographic plate. As in classical interferometry, a beam splitter initially divides the laser light into two beams. But, for holography the standard terminology is slightly different. One beam, called the reference beam, passes through the undisturbed ambient air and strikes the holographic plate. The other beam, called the object beam, passes through the test section prior to reaching the plate. When holography is applied to the measurement of refractive index fields, the test fluid is called a phase object. This is because the test fluid mainly affects the phase distribution of the light beam.

As discussed in the previous section, a classical interferogram is formed by the interference of the test beam with the reference beam, while the heat transfer process of interest is occurring in the test beam. In contrast, for holographic interferometry, the interferogram is generated by the interference of two object beams, which occur at different times. Two object waves, one with and one without heat transfer, are superposed to produce the interferogram. Two methods are commonly used to achieve this superposition: (i) Double Exposure holographic interferometry and, (ii) Real-time holographic interferometry.

Both the Double Exposure and Real-time methods make use of object beam reconstruction. As illustrated in Figure 6, a hologram of the phase object will reconstruct the object wave when it is re-illuminated with the reference wave. A heated model is shown in the object beam, as an example. In Figure 6(a), a holographic plate is first illuminated by both the plane reference wave and the object wave, which has passed by the heated model. As discussed in Section 2, when two coherent light beams intersect, a fringe pattern will be formed. This

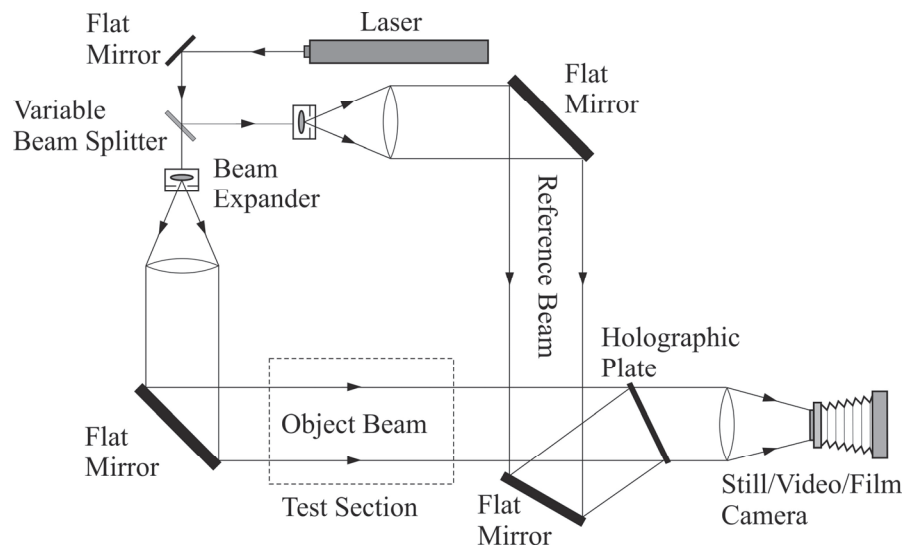


Figure 5: Typical optical setup of a holographic interferometer for the measurement of convective heat transfer [36].

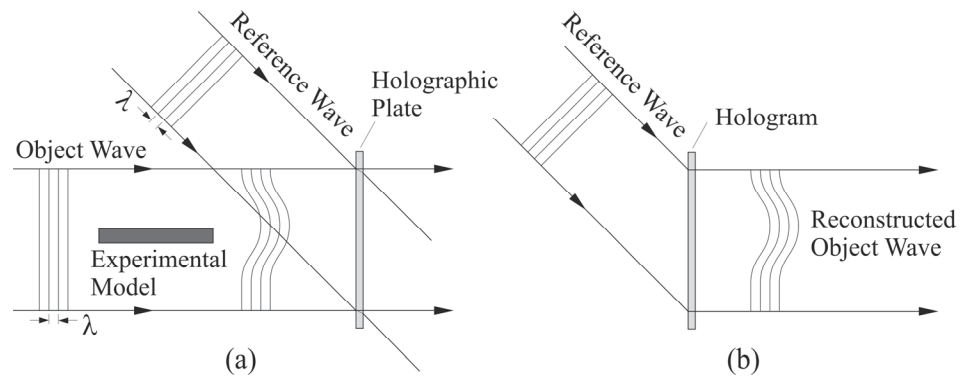


Figure 6: Illustration of the object wave reconstruction by a hologram.

pattern will consist of a microscopic finite fringe pattern, which will be recorded on the light sensitive emulsion. After developing and fixing, the fringe pattern is permanently recorded on the plate, and the plate is called a hologram. As shown in Figure 6(b), if this hologram is now illuminated with the same reference beam, the hologram behaves like a complex diffraction grating and the original object beam is “reconstructed” i.e., the object beam, containing all the original phase and amplitude information, is emitted from the back of the hologram. This phenomenon was discovered in 1948 by Gabor [26, 27, 28] and forms the basis of holography. A more detailed discussion of diffraction gratings and the optics of beam reconstruction is given by Vest [21].

Two important features of the fringe pattern that is recorded on the hologram should be clarified. First, unlike the macroscopic fringes on a typical finite fringe interferogram, the fringe pattern recorded on the hologram will not be visible to the naked eye. Typically, the fringe density will be of the order of 1000 fringes per millimeter or more. Second, in contrast to the uniform diffraction grating formed by two intersecting plane waves (as in Figure 3), the microscopic fringe pattern on the hologram will be highly complex because of the refractive index variation in the phase object.

3.1 Double exposure holographic interferometry

In the double exposure method, two different object beams are recorded on the same holographic plate using multiple exposures. The steps are shown in Figure 7. First the holographic plate is exposed to the object beam with the experimental model at thermal equilibrium with the surroundings. Note that this object wave, called the comparison wave, will be affected by imperfections in optical components such as mirrors and optical windows. Then, the model is heated (or cooled) to the desired test condition and the holographic plate is exposed for the second time. This second object wave, called the measurement wave, is stored on the plate and will be affected by both the optical imperfections and the refractive index variations in the experimental model. The holographic plate is then developed and repositioned in the interferometer. When this multiple exposure hologram is illuminated by the reference wave both object waves are reconstructed simultaneously. Because the phase difference between the comparison wave and the measurement wave is produced only by the variations of refractive index in the phase object, the output will be an interference pattern which is unaffected by optical imperfections. If the angle between the object beam and reference beam remains identical during exposure to both the comparison and measurement waves, an infinite fringe pattern will be obtained. But, if the angle between the object and reference beam is adjusted slightly between exposures, a finite fringe pattern can be obtained.

The double exposure method has been used frequently for convective heat transfer studies [29, 30, 31]. The main advantage of this method is primarily its simplicity. However, the main drawback is that it produces a static interferogram, which cannot be seen until the plate is developed. So, transient processes cannot be observed continuously in real-time, as in classical interferometry. Also, this

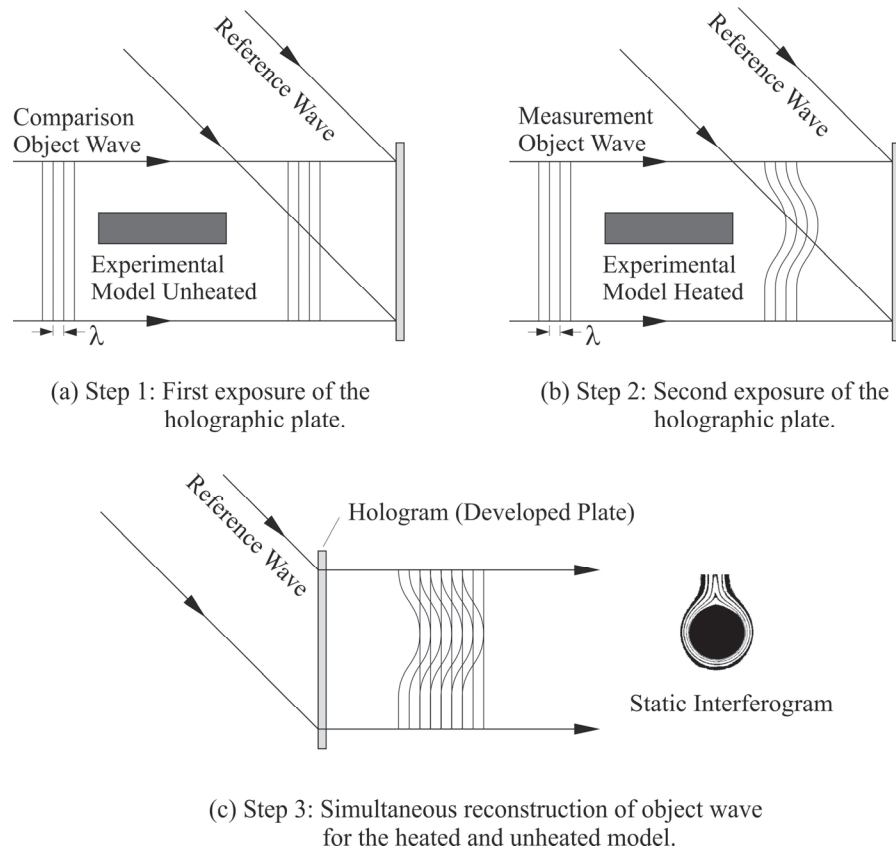
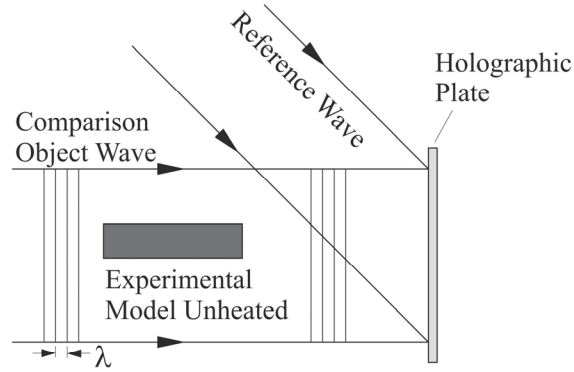


Figure 7: Steps in double exposure holographic interferometry.

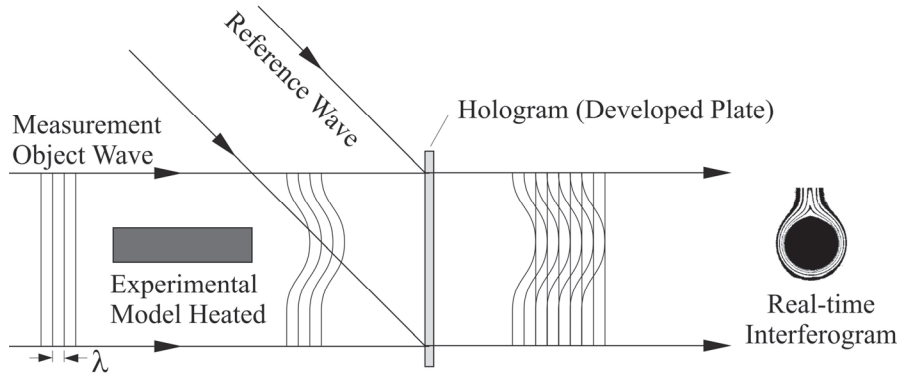
method has the disadvantage that a separate holographic plate is required for each test condition. These problems can be avoided by the use of the real-time method, which is described in the next section.

3.2 Real-time holographic interferometry

As the name implies, the real-time method permits continuous observation of the temperature field in the experimental model. Figure 8 illustrates the steps in the real-time method. The first step is that the holographic plate is exposed to the unheated model i.e., the comparison wave and reference wave. The plate, with this single exposure, is then developed. The next step is that the experimental model is heated to the desired conditions. The hologram is repositioned in the interferometer and is illuminated with the new object wave and the reference wave. The measurement wave passes through the hologram and interferes with the



(a) Step 1: Recording of the undisturbed comparison object wave on the holographic plate.



(b) Step 2: Interference of the reconstructed comparison object wave with the instantaneous object wave with the heated model.

Figure 8: Steps in real-time holographic interferometry.

comparison wave of the unheated model, which is reconstructed by the reference wave. The resulting output is a continuous infinite fringe interference pattern, which can be observed in real time. As with the double exposure method, if desired, a finite fringe pattern can be obtained by adjusting the angle slightly between the reference and object (measurement) waves.

Many studies have applied the real-time method for free and forced convective heat transfer measurements [32, 33, 34, 35]. From the above discussion it is clear that the real-time method overcomes many of the limitations of the double exposure method. The method allows continuous measurements of transient processes and a single holographic plate can be used to study a range of test conditions. However, one difficulty of the real-time method is that after

processing, the hologram must be returned precisely to the location where it was initially exposed, to within a fraction of a wavelength. Otherwise, fringes will appear in the output that are caused by the hologram's displacement. Mayinger [36] recommends the use of a mounting frame with three electrically-driven piezo-quartz devices for fine repositioning. Another method of overcoming this problem is to chemically process the plate in situ, by mounting it inside a special transparent cuvette [21].

It should be clear from the descriptions of the double exposure and real-time methods that the optical components of a holographic interferometer do not require the same precision as those of a MZI. Because both the comparison and measurement waves are affected in precisely the same way by any optical imperfections, the phase difference between the two beams is caused only by refractive index variations in the test section. So, for example, standard commercial glass can be used instead of precision optical windows to seal off the ends of a test model. In fact, the ability to use much cheaper optical components is one reason for the recent increase in the popularity of holographic interferometry, which is now more common than classical interferometry.

4 Interferogram analysis

In general, the analysis of interferograms is identical for both holographic and classical interferometry. Interferometry utilizes the wave nature of light. The amplitude of a monochromatic light wave propagating in the z direction can be expressed as a function of position (z) and time (t) as follows:

$$A = A_o \sin\left(\frac{2\pi}{\lambda}(ct - z)\right) \quad (2)$$

where A_o is the maximum amplitude, c the speed of light and λ the wavelength. So, the amplitude of one wave at a fixed point in space can be expressed as:

$$A_1 = A_{o,1} \sin\left(\frac{2\pi ct}{\lambda}\right) \quad (3)$$

Similarly, amplitude of a second wave at the same z location can be represented by:

$$A_2 = A_{o,2} \sin\left(\frac{2\pi ct}{\lambda} - \phi\right) \quad (4)$$

where ϕ is the phase shift between the two waves, caused by the change in refractive index of the fluid in the experimental model.

Now consider these two beams recombining in the output of an interferometer. Assuming the maximum amplitude of both waves to be the same ($A_{o,1}=A_{o,2}=A_o$), eqns (3) and (4) can be summed, as follows:

$$A_{\text{tot}} = A_o \left(\sin\left(\frac{2\pi ct}{\lambda}\right) + \sin\left(\frac{2\pi ct}{\lambda} - \phi\right) \right) \quad (5)$$

It is evident that constructive interference will occur when $\phi/2\pi$ is an integer and destructive interference will result when $(\phi/2\pi) + 1/2$ is an integer. Thus, from fringe center to fringe center, a phase difference equivalent to one wavelength exists between the two beams.

The phase shift between the reference and test beams is related to the difference in the number of waves in the two beams, as follows:

$$\frac{\phi}{2\pi} = \int_1 \frac{dz}{\lambda} - \int_2 \frac{dz}{\lambda} \quad (6)$$

where λ is the local wavelength, which can vary along the light path. Physically, the two integrals on the right hand side of eqn (6) represent the number of light waves in beam 1 and beam 2.

An interferometer measures the phase shift between two light waves, which is caused by changes in the refractive index in the experimental model. Refractive index (n) of a medium is defined as the ratio of the speed of light in a vacuum (c_o) to the speed of light in the medium (c):

$$n = \frac{c_o}{c} = \frac{\lambda_o}{\lambda} \quad (7)$$

Solving eqn (7) for λ and substituting the result into eqn (6) gives:

$$\varepsilon = \frac{\phi}{2\pi} = \frac{1}{\lambda_o} \left[\int_1 n \, dz - \int_2 n \, dz \right] \quad (8)$$

where ε is the fringe shift order. It should be mentioned that in the field of optics the integral of the refractive index along a light path is called the *optical path length* (S), and defined as follows:

$$S = \int n \, dz = c_o \int \frac{dz}{c} = \lambda_o \int \frac{dz}{\lambda} \quad (9)$$

So, comparing eqns (8) and (9), the fringe shift order can be expressed in terms of the difference in optical path length of two beams:

$$\varepsilon = (S_1 - S_2) / \lambda_o \quad (10)$$

For classical interferometry, the integrals in eqn (8) correspond to the test and reference beams. In holographic interferometry, the integrals correspond to the

comparison and measurement object beams, which occur at different times. In either case, the refractive index of one beam is a known constant value, n_{ref} . So, the fringe shift can be expressed as follows:

$$\varepsilon = \frac{1}{\lambda_o} \left[\int_0^L (n_{\text{ref}} - n) dz \right] \quad (11)$$

where L is the length of the test beam over which the refractive index varies. Written in this form, a positive fringe shift is measured relative to the reference state in the direction of decreasing refractive index. Since the positive direction of the fringe shift order is arbitrary, eqn (11) can also be written as:

$$\varepsilon = \frac{1}{\lambda_o} \left[\int_0^L (n - n_{\text{ref}}) dz \right] \quad (12)$$

When applying eqn (12), a positive fringe shift is measured in the direction of increasing refractive index.

4.1 Analysis of two-dimensional temperature fields

As can be seen in eqns (11) and (12), the fringe field in the output of an interferometer is a measure of the change in refractive index, integrated along the light path. If the refractive index field is two-dimensional, with no variation of refractive index in the direction of the light beam, eqn (11) can be integrated over the length of the test section (L). Assuming sharp discontinuities at the entrance and exit of the test section (i.e., neglecting end effects), eqn (11) becomes:

$$\varepsilon = \frac{1}{\lambda_o} \left[\int_0^L (n_{\text{ref}} - n) dz \right] = \frac{L}{\lambda_o} (n_{\text{ref}} - n) \quad (13)$$

The refractive index (n) of both liquids and gases is directly related to density (ρ) by the Lorentz-Lorenz equation [37]:

$$\frac{n^2 - 1}{\rho(n^2 + 2)} = \bar{r} \quad (14)$$

where \bar{r} is the specific refractivity, which is a function of the substance and wavelength. For gases near room temperature and pressure, the index of refraction is very close to unity. For example, the refractive index of air at 20°C and 1 atm for He-Ne laser light is $n=1.0002716$. So, eqn (14) can be simplified as follows:

$$\frac{n^2 - 1}{\rho(n^2 + 2)} \approx \frac{2(n - 1)}{3\rho} = \bar{r} \quad (15)$$

For applications involving gases, eqn (15) is often written in the form of the Gladstone-Dale equation, as follows:

$$n - 1 = \rho G \quad (16)$$

where G is the Gladstone-Dale constant ($G = 3\bar{r}/2$). The Gladstone-Dale constant depends on the type of gas, but varies weakly with temperature, pressure and light wavelength. Values of G for several gases are given in Table 1. Values are shown for $\lambda_o=514.5$ nm and $\lambda_o=632.8$ nm, which correspond to the wavelengths of argon ion and He-Ne lasers. For mixtures of gases, the Gladstone-Dale constant can be calculated as the mass fraction weighted average of the values of the constituents [38].

Introducing the ideal gas equation of state into the Gladstone-Dale equation gives the relationship between absolute temperature (T) and index of refraction (n), as follows:

$$n = \frac{PG}{RT} + 1 \quad (17)$$

where T is the absolute temperature and R is the gas constant. Substitution of eqn (17) into eqn (13) yields an equation for determining the fringe shift between two known temperatures:

$$\varepsilon = \frac{LPG}{R\lambda_o} \left(\frac{1}{T_{\text{ref}}} - \frac{1}{T} \right) \quad (18)$$

Solving eqn (18) for temperature gives:

$$T = \frac{T_{\text{ref}}}{1 - \frac{\varepsilon R \lambda_o T_{\text{ref}}}{LPG}} \quad (19)$$

Eqn (19) can be used to calculate the fluid temperature at any location for a known fringe shift (ε) relative to a known temperature (T_{ref}). For external flow experiments, the reference temperature is often taken as the ambient temperature. However, eqn (19) can also be applied between any two points on an interferogram, provided the temperature is known at one location, which is used as the reference value. This approach is used when studying an internal flow, where the fringe shift cannot be measured relative to the ambient temperature. In this case, thermocouple measurements are used to determine the temperature of one surface, which is used as the reference.

Table 1: Gladstone-Dale constant (G) for gases near standard temperature and pressure [13, 21].

Gas	G (m ³ /kg)	
	$\lambda_0=514.5 \text{ nm}$	$\lambda_0=632.8 \text{ nm}$
Air	0.227×10^{-3}	0.226×10^{-3}
Argon, Ar	0.159×10^{-3}	0.158×10^{-3}
Carbon Dioxide, CO ₂	0.229×10^{-3}	0.227×10^{-3}
Helium, He	0.196×10^{-3}	0.195×10^{-3}
Nitrogen, N ₂	0.240×10^{-3}	0.238×10^{-3}
Oxygen, O ₂	0.191×10^{-3}	0.189×10^{-3}
Water Vapor (at 1 atm)	0.314×10^{-3}	0.312×10^{-3}

When liquids are used as the test fluid for interferometry, empirical relations can be used to relate the refractive index to temperature. For example, if water is used as the test medium, the refractive index can be approximated as follows:

$$\begin{aligned} n &= 1.332713 - (6.2344T + 2.286T^2) \times 10^{-6} + 9.005 \times 10^{-9} T^3 \quad \text{for } \lambda_0 = 632.8 \text{ nm} \\ n &= 1.336897 - (7.4862T + 2.3113T^2) \times 10^{-6} + 9.135 \times 10^{-9} T^3 \quad \text{for } \lambda_0 = 514.5 \text{ nm} \end{aligned} \quad (20)$$

where T is in degrees Celsius. These equations are best fit curves to the data of Tilton and Taylor [39] over the temperature range 0°C to 60°C. Dobbins and Peck [40] have also developed empirical relations based on more detailed measurements of the refractive index of water at $\lambda_0 = 632.8 \text{ nm}$ over the temperature range 20°C to 35°C.

In cases where the detailed variation of refractive index with temperature is not known, an approximate method can be used. Over small temperature differences, eqn (13) may be approximated by:

$$\varepsilon = \frac{L}{\lambda_0} \frac{\partial n}{\partial T} (T_{\text{ref}} - T) \quad (21)$$

Solving for temperature:

$$T = T_{\text{ref}} - \frac{\lambda_0 \varepsilon}{L \frac{\partial n}{\partial T}} \quad (22)$$

Eqn (22) can be applied for a known rate of change of refractive index with temperature, $\partial n / \partial T$. Table 2 gives values of $\partial n / \partial T$ for various liquids at 25°C. In cases where $\partial n / \partial T$ data are not available, Murphy and Alpert [41] have shown that the following approximate expression can be used:

$$\frac{\partial n}{\partial T} = -\frac{3}{2} \left[\frac{n(n^2 - 1)}{2n^2 + 1} \right] \beta \quad (23)$$

where β is the coefficient of volumetric expansion of the liquid. Murphy and Alpert compared eqn (23) to experimental data for a several fluids. Predicted values of $\partial n/\partial T$ were 2 percent lower on average than measured values.

Once the temperature field in the gas or liquid has been obtained, the local heat flux can be calculated using Fourier's law. At the surface the fluid velocity is zero and heat is transferred to the fluid by pure conduction. So, the local heat flux (q) is given by:

$$q = -k_s \left. \frac{dT}{dx} \right|_{x=0} \quad (24)$$

where k_s is the conductivity of the fluid evaluated at the surface temperature and x is the coordinate normal to the surface.

Often the local convection coefficient is of interest. Using this heat flux, the local convection coefficient (h) can be evaluated as:

$$h = \frac{-k_s dT/dx|_{x=0}}{T_s - T_\infty} \quad (25)$$

where T_s is the local surface temperature and T_∞ is the ambient or bulk fluid temperature, as appropriate.

In eqns (24) and (25) the temperature gradient at the surface is required to calculate the local heat transfer rate. A common method to obtain the gradient is to evaluate the fringe temperatures along a straight line taken perpendicular to the surface. Using discrete temperature profile data, usually taken at fringe centers, a curve-fitting algorithm is then used to get the temperature gradient at the surface. Various extrapolation schemes have been proposed. For example, Khuen and Goldstein [42] have obtained excellent results with linear extrapolation using the two fringes closest to the surface. In contrast, McAuliffe and Wirtz [43] recommend a least square fit using a third order polynomial. For measurements on cylindrical surfaces with low radius of curvature, Eckert and Soehngen [2] have shown that extrapolation should be based on the logarithm of radius.

Small phase differences can be measured using specialized optical methods (Slepicka and Cha [44], Breuckmann and Thieme [45]). But when interference patterns are recorded on film, several fringes are needed near the surface in order to characterize the near-wall temperature profile. Unfortunately, because of the large variation in local heat transfer rates that is often encountered in a single experimental model, this is not always possible. Often, in regions with low local heat transfer rates there is insufficient fringe shift close to the surface. In such

Table 2: Rate of change of refractive index with temperature of various liquids at 25°C [13, 21].

Liquid	$-\partial n / \partial T \times 10^4 \text{ (K}^{-1}\text{)}$	
	$\lambda_o=546.1 \text{ nm}$	$\lambda_o=632.8 \text{ nm}$
Water	1.00	0.985
Methyl alcohol	4.05	4.0
Ethyl alcohol	4.05	4.0
Isopropyl alcohol	4.15	4.15
Benzene	6.42	6.40
Toluene	5.55	5.55
Nitrobenzene	4.68	4.68
c-Hexane	5.46	5.43
n-Hexane	5.43	5.4
n-Octane	4.76	--
n-Decane	4.48	--
n-Hexadecane	4.06	--
Isooctane	4.87	--
Acetone	5.31	5.31
Chloroform	5.98	5.98
Carbon tetrachloride	5.99	5.98
Carbon disulfide	7.96	7.96

locations, it is possible to measure the gradient *directly* from the interference fringe field. This method is discussed in the next section.

4.1.1 Direct gradient measurement

To measure the surface temperature gradient directly, the interferometer is operated in the finite fringe mode. Consider a measurement being made on a vertical surface, as shown in Figure 9(a). For a two-dimensional field, with a finite fringe spacing in the y-direction of $d=\lambda/\theta$, the fringe shift is related to the refractive field (to within a constant) as follows:

$$\varepsilon(x, y) = \frac{L}{\lambda_o} (n_\infty - n(x, y)) \pm \frac{y\theta}{\lambda} \quad (26)$$

where the x-axis is perpendicular to the solid-fluid interface and the y-axis is parallel to the interface. For generality, the last term in eqn (26) is shown as plus or minus. The sign depends upon whether the test beam is angled downward or upward relative to the reference beam. For the current analysis, the term $y\theta/\lambda$ will be taken as positive. For this optical setting, when the undisturbed wedge fringes in the ambient are perpendicular to the vertical surface ($\gamma=90^\circ$), a negative temperature gradient in the x-direction will cause the finite fringes to bend downward near the surface, as shown in Figure 9.


$$\frac{\partial \varepsilon}{\partial x} = \frac{-L}{\lambda_o} \frac{\partial n}{\partial x} = \frac{-L}{\lambda_o} \frac{\partial n}{\partial T} \frac{\partial T}{\partial x} \quad (27)$$
$$\frac{\partial \Gamma}{\partial \mathbf{x}} = \frac{-\lambda_o}{L} \frac{\partial \varepsilon / \partial \mathbf{x}}{\partial \mathbf{n} / \partial \Gamma} \quad (28)$$
$$\frac{\partial n}{\partial T} = \frac{-P G}{RT^2} \quad (29)$$
$$\left. \frac{\partial T}{\partial x} \right|_{x=0} = \frac{R \lambda_o T_s^2}{L P G} \left. \frac{\partial \varepsilon}{\partial x} \right|_{x=0} \quad (30)$$

The fringe shift gradient parallel to the surface is obtained by differentiating eqn (26) with respect to y and substituting eqn (17):

$$\left. \frac{\partial \varepsilon}{\partial y} \right|_{x=0} = \frac{LPG}{R \lambda_o T_s^2} \frac{\partial T_s}{\partial y} + \frac{1}{d} \quad (31)$$

Consider an incremental fringe shift along a line in the x-direction as shown in Figure 9(b). Applying eqn (31) for an isothermal surface ($dT_s/dy=0$), the incremental fringe shift will be $d\varepsilon = dy/d$. Noting that $\tan(\alpha)=-dx/dy$, the fringe shift gradient in the x-direction can be expressed as:

$$\left. \frac{\partial \varepsilon}{\partial x} \right|_{x=0} = \frac{-1}{d \tan \alpha} \quad (32)$$

where α is the angle between a line of constant fringe shift and the surface at $x=0$. Substituting eqn (30) into eqn (24) gives the local heat flux:

$$q = -k_s \left. \frac{\partial T}{\partial x} \right|_{x=0} = h(T_s - T_\infty) = \frac{k_s R \lambda_o T_s^2}{LPG d \tan \alpha} \quad (33)$$

Rearranging eqn (33) gives an expression for the local heat transfer coefficient (h):

$$h = \frac{k_s R \lambda_o T_s^2}{LPG (T_s - T_\infty) d \tan \alpha} = \frac{C}{\tan \alpha} \quad (34)$$

where $C=(k_s R \lambda_o T_s^2)/(LPG(T_s - T_\infty)d)$ is a constant for a given interferogram. Using eqn (34), the local heat transfer coefficient can be obtained by measuring the angle (α) between a line of constant fringe shift and an isothermal surface. Figure 10 shows the variation of h/C with the intersection angle (α) of the wedge fringe and surface.

Figure 11 shows a sample application that is well suited for analysis by the direct gradient method [46]. Figure 11(a) shows an infinite fringe interferogram and Figure 11(b) shows the same experimental conditions taken in finite fringe mode. These are interferograms of the temperature field in air adjacent to a window glazing with a Venetian blind. The blind slats (seen edge on) are heated electrically to simulate solar irradiation. In the middle and upper part of the infinite fringe interferogram, there is insufficient fringe shift near the window surface to obtain reliable measurements. However, in the wedge fringe interferogram the variation of the fringe angle (α) at the window surface is clearly visible and can be measured. In fact, the wedge fringe pattern also provides better visualization of the local heat transfer distribution than the infinite fringe pattern. On the lower part of the window the fringe angle (α) is less than 90° , indicating that heat is being transferred from the window to the air. Further up the window the fringes intersect the surface at almost 90° , indicating that the surface is nearly adiabatic. At the top of the interferogram, the intersection angle is greater than 90° , revealing that direction of heat flow has reversed.

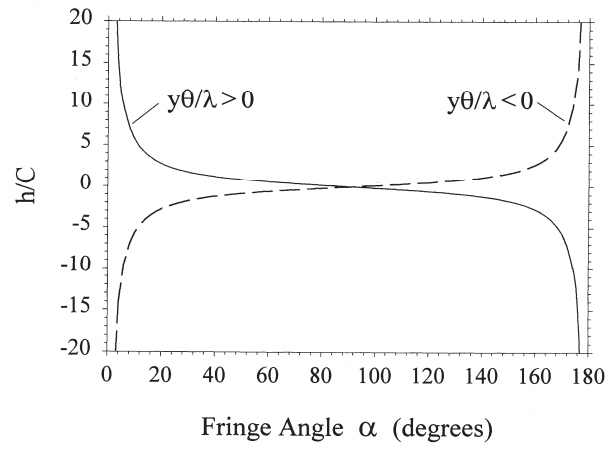


Figure 10: Variation of the local heat transfer coefficient with fringe/surface intersection angle (α).

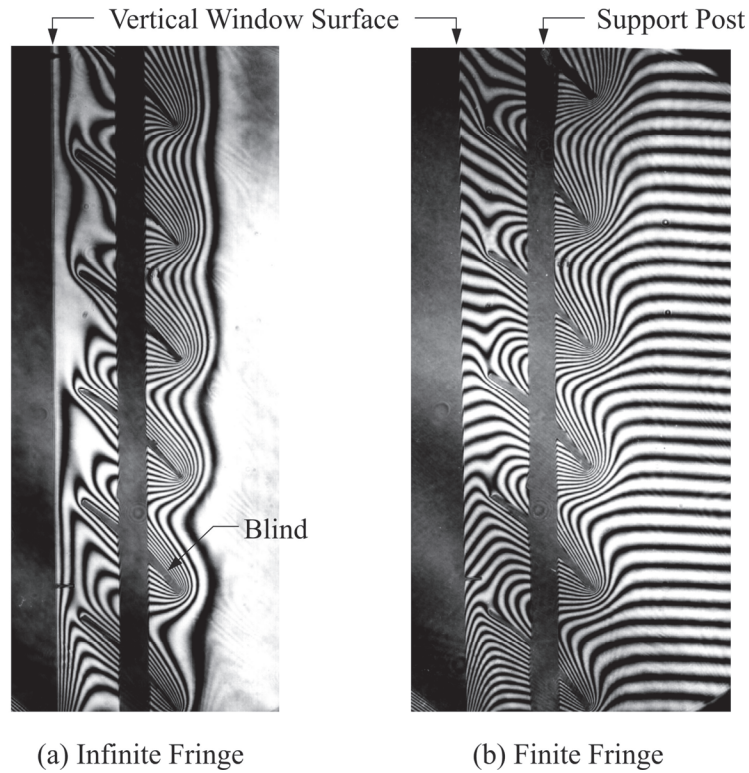


Figure 11: Interferograms of free convection from a window with a heated Venetian blind, illustrating an application of the direct gradient method [46].

Naylor and Duarte [47] have shown that uncertainty in the measurement of the fringe angle can be a significant source of error in this method. To minimize this experimental uncertainty, the fringe angle sensitivity coefficient $\partial h/\partial \alpha$ should be minimized. Differentiating eqn (34) gives this sensitivity coefficient:

$$\frac{\partial h}{\partial \alpha} = \frac{-k_s R \lambda_o T_s^2}{L P G (T_s - T_\infty) d} \left(\frac{1 + \tan^2 \alpha}{\tan^2 \alpha} \right) \quad (35)$$

Figure 12 shows the variation of the fringe angle sensitivity coefficient and surface temperature gradient with fringe angle (α) for a wedge fringe spacing of $d=2$ mm. For the other parameters, typical values for an experimental setup have been used. The magnitude of the sensitivity coefficient is a minimum at $\alpha=90^\circ$, and has a relatively flat behaviour in the range $50^\circ < \alpha < 130^\circ$, which represents the most desirable measurement range for $d=2$ mm. The corresponding temperature gradient variation has also been plotted in Figure 12. It can be seen that the region of relatively low sensitivity to fringe angle ($50^\circ < \alpha < 130^\circ$) corresponds to a surface temperature gradient range of approximately $-1250 \text{ K/m} \leq \partial T/\partial x \leq 1250 \text{ K/m}$, indicating that this method will give the most accurate results in regions with relatively low heat transfer rates. Since the need for this analysis method exists primarily where the temperature gradient is low, this is very fortunate behaviour.

When using the direct gradient method, the wedge fringe spacing (d) should be adjusted to minimize the sensitivity coefficient $\partial h/\partial \alpha$. As previously discussed, for conventional interferometry, this is done by adjusting the recombination angle of test beam and reference beam. For double exposure holographic interferometry, the wedge fringe spacing is set by changing the angle between the object beam and reference beam between exposures. It has been shown [47] that the optimum wedge fringe spacing (d_{opt}) that minimizes the fringe angle sensitivity coefficient is:

$$d_{\text{opt}} = \frac{R \lambda_o T_s^2}{L P G \left| \frac{\partial T}{\partial x} \right|_{x=0}} \quad (36)$$

Using eqn (36), the optimum fringe spacing can be set for each interferogram, provided that an estimate can be made of the temperature gradient to be measured.

The variation of fringe angle sensitivity coefficient with fringe spacing is shown in Figure 13. The line of optimum fringe spacing (eqn (36)) is also shown for a typical set of experimental conditions. It can be seen that for higher temperature gradients, the sensitivity coefficient has a pronounced minimum. However, at lower gradients the optimum fringe spacing (d) is less clearly defined. This “flat” behaviour at low gradients is desirable because a single fixed fringe spacing (i.e. a single interferogram) can be used to make measurements over a range of gradients without greatly compromising the level of experimental uncertainty.

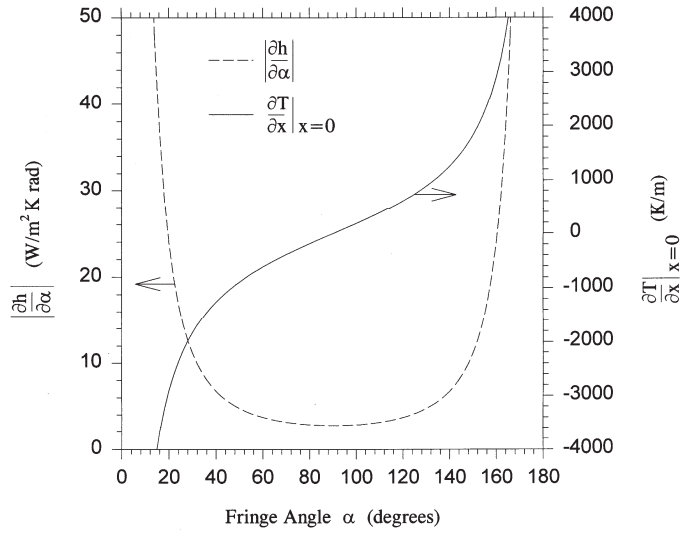


Figure 12: Fringe angle sensitivity coefficient and temperature gradient variation with fringe angle for typical experimental conditions in air ($d=2$ mm, $L=0.355$ m, $P=100$ kPa, $T_s=305$ K, $T_\infty=295$ K, $\lambda_o=632.8$ nm).

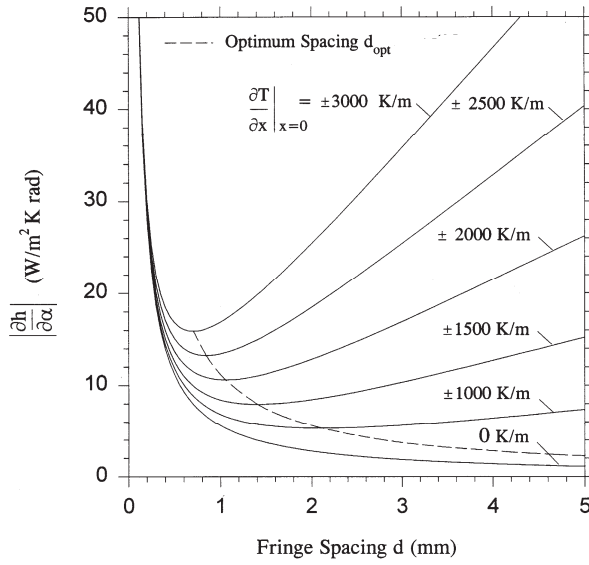


Figure 13: Effect of fringe spacing on the fringe angle sensitivity coefficient for typical experimental conditions in air ($L=0.355$ m, $P=100$ kPa, $T_s=305$ K, $T_\infty=295$ K, $\lambda_o=632.8$ nm).

$$\Delta\epsilon_{AB} \approx \frac{w_2}{w_1 + w_2} \quad (37)$$

$$\Delta\epsilon_{AB} \approx \frac{w_2}{w_1 + w_2} \quad (37)$$

Solid-Fluid Interface

Undisturbed Fringe

w_1

w_2

B

A

d

$\gamma = 90^\circ$

Uniform Ambient Temperature T_∞

y

x

Figure 14: Measurement of partial fringe shift using finite fringes [12].

4.1.2 Refraction effects

In deriving the equations in the preceding sections it has been assumed that the light rays passing through the experimental test section travel in straight lines; in fact, when heat transfer is occurring, a light ray will curve slightly as it passes through the experimental model because of refractive index gradients perpendicular to the direction of propagation.

Refraction of the light beam as it passes through the test section causes two deviations from the ideal evaluation equations. One source of refraction error is the displacement of the beam, which can lead to errors in the x-y position assigned to the fringe locations. This error can be reduced greatly by focusing the camera at the center of the test model [12, 13]. The second source of refraction error is that the light ray does not travel along a straight line of constant refractive index in a two-dimensional field, as assumed in the ideal evaluating equations.

By integrating the refractive index variation along the curved optical path, Hauf and Griggull [13] have obtained the following expression for the fringe shift, including refraction effects:

$$\varepsilon = \frac{(n_{\infty} - n)L}{\lambda_o} + \Delta\varepsilon_r \quad (38)$$

$$\text{where } \Delta\varepsilon_r = -\frac{L^3}{12\lambda_o n} \left(\frac{\partial n}{\partial x} \right)^2 = -\frac{L^3}{12\lambda_o n} \left(\frac{\partial T}{\partial x} \right)^2 \left(\frac{\partial n}{\partial T} \right)^2$$

where $\Delta\varepsilon_r$ is the addition fringe shift caused by refraction. In deriving this equation, it was assumed that the camera was focused at the center of the test section in order to minimize the fringe displacement error. Also, the approximation was made that $\partial n / \partial x = \text{constant}$ along the curved optical path, such that a light ray follows a parabolic trajectory.

Rearranging eqn (21), the temperature difference (ΔT) associated with an incremental fringe shift ($\Delta\varepsilon$) can be expressed as:

$$\Delta T = \frac{\lambda_o}{L} \frac{\Delta\varepsilon}{\partial n / \partial T} \quad (39)$$

Substituting eqn (38) into eqn (39) gives an approximate correction for refraction, that can be applied to the fringe temperatures [12]:

$$\Delta T = \frac{-L^2}{12n} \frac{\partial T}{\partial n} \left(\frac{\partial T}{\partial x} \right)^2 \quad (40)$$

It should be emphasized that eqn (40) applies only when refraction errors are small. When large refraction effects are present, special reconstruction techniques are required, since both the path of the light and the refractive index fields are unknown. The reader is referred to interferometric measurements that have been

made in the presence of strong refraction by Lacona and Taine [48] and Dietz and Balkowski [49].

Depending upon the specific situation, corrections for other sources of error should also be considered. These include the additional fringe shift caused by end effects [12, 13, 50] and errors caused by slight test section misalignment with the object/test beam [51]. In addition, if the test model requires the use of optical windows, the additional fringe shift caused by the free convective boundary layers on the outside of the windows should be considered.

4.2 Analysis of three-dimensional temperature fields

In a three-dimensional temperature field, neglecting refraction effects, the fringe shift $\epsilon(x,y)$ depends on the refractive index field $n(x,y,z)$ as follows:

$$\epsilon(x,y) = \frac{1}{\lambda_o} \int (n(x,y,z) - n_{\text{ref}}) dz \quad (41)$$

where z is the direction of light propagation. For a general three-dimensional field, inversion of this line integral transform is not possible from a single interferogram. Estimation of the refractive index field requires several interferograms, each recorded at a different viewing angle relative to the phase object. Tomographic methods are then applied to the two-dimensional fringe data from the multiple views to reconstruct the temperature field. The reader is referred to reference [21] for a discussion of the fundamentals of interferometric tomography.

In practice, the accuracy of the reconstructed temperature field depends upon the degree to which the view is unobstructed. For example, substantial success has been achieved in reconstructing thermal plumes where a full 180 degree range of viewing angle was available [52, 53]. For example, Bahl and Liburdy [52] have used tomography to reconstruct the plume above a heated disk. In this study the local heat transfer coefficient distribution on the disk was obtained from the temperature field. Recently, Mishra et al. [4] have used tomography to study Rayleigh-Benard convection in a horizontal bottom-heated enclosure with air as the test fluid. Again, in this case, data from a wide range of viewing angles could be obtained. However, for many practical geometries, the opaque test model blocks the light beam and only a limited range of view is available. In such cases, the reconstruction problem becomes ill-posed and is substantially more difficult [54]. Some recent work (which was only partly successful) has been done on reconstruction methods with a limited range of view [31, 55] using holographic interferometry. Reference [73] gives a brief review of this research.

4.2.1 Radially symmetric fields

In the special case of a radially symmetric phase object, the temperature field can be reconstructed from a single interferogram. This case is commonly encountered in the study of such problems as jets, flames, bubbles, and free convection from vertical cylinders and cones. As shown in Figure 15, consider the cross section of a field where the refractive index is only a function of r in the x - z plane. The

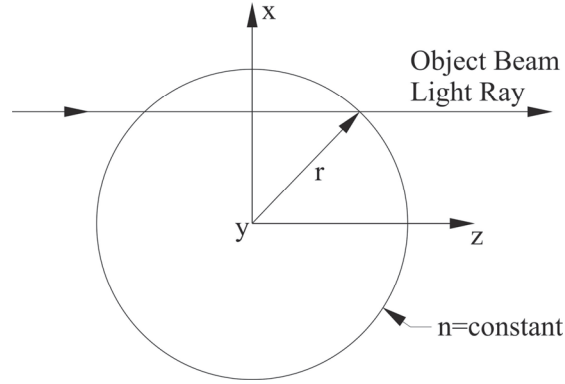


Figure 15: Cross section of a radially symmetric refractive index field.

refractive index may also be a function of the axial coordinate y , but not of angular position. The object/test beam passes through the field in the z direction. Noting that $z=(r^2-x^2)^{1/2}$, at constant x :

$$dz = \frac{r dr}{\sqrt{r^2 - x^2}} \quad (42)$$

Substituting eqn (42) into eqn (41), the fringe shift can be expressed as:

$$\varepsilon(x) = \frac{2}{\lambda_o} \int_x^{+\infty} \frac{(n(r) - n_{\text{ref}}) r dr}{\sqrt{r^2 - x^2}} \quad (43)$$

The integral on the right hand side of eqn (43) is the Abel transform. Although the upper limit on the integral is shown as $+\infty$, in practice integration is terminated at the location where $n(r)-n_{\text{ref}}=0$, within the accuracy of the experimental data. This integral equation can be solved numerically, given fringe shift data at discrete locations [13, 21, 56]. Alternately, eqn (43) can be solved using the Abel inversion:

$$n(r) - n_{\text{ref}} = \frac{\lambda_o}{\pi} \int_r^{+\infty} \frac{(\partial \varepsilon / \partial x) dx}{\sqrt{x^2 - r^2}} \quad (44)$$

A derivation of this inversion formula has been presented by Goldstein [12] and several numerical methods for integrating eqn (44) have been reviewed by Vest [21]. One drawback of using the Abel inversion is that differentiation of the experimental fringe data ($d\varepsilon/dx$) is required. Merzkirch [38] notes that differentiation tends to amplify data noise and can lead to considerable experimental error.

4.2.2 Beam-averaged local measurements

As stated previously, for an asymmetric three-dimensional field, the temperature field cannot be determined from a single interferogram. However, for some geometries, it is possible to determine the “local” convective heat transfer rate that is averaged in the direction of the light beam.

Figure 16 shows two interferograms of three-dimensional thermally developing flow taken with a MZI. Figure 16(a) is a beam-averaged interferogram of free convection from an upward-facing heated plate, inclined at 18.5° from horizontal [57]. Figure 16(b) shows developing free convection in an isothermal square duct inclined at an angle of 45° with respect to gravity [58]. To obtain these infinite fringe interferograms, the test beam was passed axially along the experimental model, parallel to the direction of the primary flow. As a result, the temperature field is integrated from the inlet to the outlet of test section such that each fringe represents *approximately* a line of constant axially averaged temperature. In Figure 16(a) one can see the strong effect of longitudinal vortices on the span-wise heat transfer distribution. In Figure 16(b), it can be seen that the heat transfer rate is much lower on the upper surface of the duct than on the lower surface, because of the strong buoyancy-induced secondary flow.

To analyze this situation, consider thermally developing flow over a surface of length L , with temperature varying in the direction of the object/test beam as shown in Figure 17. The fluid temperature is T_∞ at $z=0$ and T_h at $z=L$. For simplicity, Figure 17 shows a two-dimensional convective heat transfer geometry. But, the current analysis does not preclude a temperature variation in the y -direction and can be applied to a wide variety of three-dimensional problems. For this problem, the local heat transfer rate averaged in the direction of the beam (\bar{q}) can be expressed as:

$$\bar{q} = \frac{1}{L} \int_0^L -k_s \left. \frac{\partial T}{\partial x} \right|_{x=0} dz \quad (45)$$

where $T=T(x,z)$ is the temperature field in the fluid and k_s is the fluid thermal conductivity, evaluated at the local surface temperature. If the fluid conductivity is assumed to be constant, eqn (45) becomes:

$$\bar{q} = -\frac{k_s}{L} \int_0^L \left. \frac{\partial T}{\partial x} \right|_{x=0} dz = -k_s \left[\frac{\partial}{\partial x} \int_0^L T dz^* \right]_{x=0} \quad (46)$$

where the dimensionless axial coordinate $z^*=z/L$ has been introduced. Noting that the integral on the right hand side of eqn (46) is the axially averaged fluid temperature (z -direction), eqn (46) can be written as:

$$\bar{q} = -k_s \left. \frac{\partial \bar{T}}{\partial x} \right|_{x=0} \quad \text{where} \quad \bar{T} = \int_0^1 T(x, z^*) dz^* \quad (47)$$

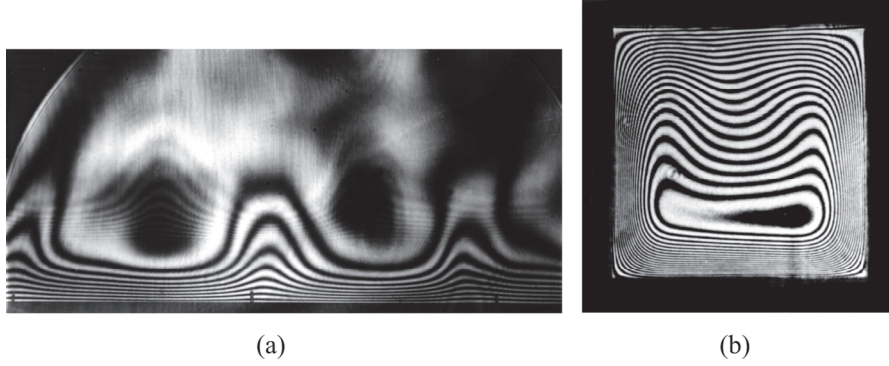


Figure 16: Beam-averaged infinite fringe interferograms of (a) free convection from an upward-facing heated plate inclined at 18.5° from the horizontal [57], and (b) developing free convection in a square duct inclined at 45° [58].

So, the heat flux on the surface can be calculated from the gradient of the average fluid temperature (\bar{T}) . The fluid conductivity in eqn (47), should be evaluated at the local axially averaged surface temperature (\bar{T}_s) .

However, Frank [59] has shown that when there is a temperature variation in the light beam direction, the temperature of a fringe calculated using eqn (19) is not exactly the arithmetic average temperature. This is because the refractive index varies non-linearly with temperature. The effective fringe temperature can be derived as follows: Consider a ray of light in the object beam passing at a distance x above the surface, as in Figure 17. Neglecting refraction effects, for an ideal gas the fringe shift is related to the temperature field by:

$$\epsilon(x) = \frac{L}{\lambda_o} \int_0^1 (n_\infty - n(x, z^*)) dz^* = \frac{LPG}{R \lambda_o} \int_0^1 \left(\frac{1}{T_\infty} - \frac{1}{T(x, z^*)} \right) dz^* \quad (48)$$

Now consider the hypothetical uniform temperature (\bar{T}_f) along the light ray that would produce the same total fringe shift $\epsilon(x)$ as the non-uniform distribution $T(x, z^*)$. With this uniform temperature, \bar{T}_f , the fringe shift is:

$$\epsilon(x) = \frac{LPG}{R \lambda_o} \int_0^1 \left(\frac{1}{T_\infty} - \frac{1}{\bar{T}_f} \right) dz^* = \frac{LPG}{R \lambda_o} \left(\frac{1}{T_\infty} - \frac{1}{\bar{T}_f} \right) \quad (49)$$

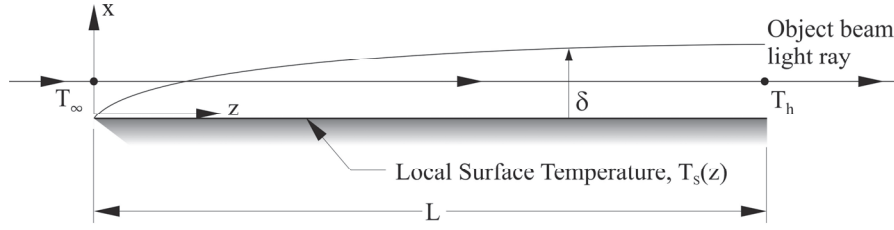


Figure 17: Thermally developing flow over a surface with a temperature variation in the light beam direction.

Equating eqns (48) and (49) and simplifying gives:

$$\bar{T}_f = \left[\int_0^1 \frac{1}{T(x, z^*)} dz^* \right]^{-1} \quad (50)$$

Eqn (50) gives the effective temperature that should be assigned to a fringe when the temperature varies in the object/test beam direction. Of course, in general, $T(x, z^*)$ is not known and cannot be determined from a single interferogram. In several previous studies [60, 61, 62], the approach taken to overcome this difficulty has been to assume that \bar{T}_f is equal to the arithmetic mean fluid temperature, \bar{T} . But, it is clear from eqn (50) that the effective fringe temperature \bar{T}_f is not the arithmetic average of $T(x, z^*)$, integrated along the light beam.

To evaluate the magnitude of the error associated with the approximation that $\bar{T}_f \approx \bar{T}$, consider a temperature variation along the object beam (for a fixed value of x) of the following form:

$$T(z^*) = (T_h - T_\infty)(z^*)^m + T_\infty \quad (51)$$

where T_∞ and T_h are the gas temperatures where the light ray enters and exits the test model, as shown in Figure 17. For the variation given in eqn (51), the average temperature along the length of the beam is:

$$\bar{T} = \int_0^1 T(z^*) dz^* = \frac{(T_h - T_\infty)}{m+1} + T_\infty \quad (52)$$

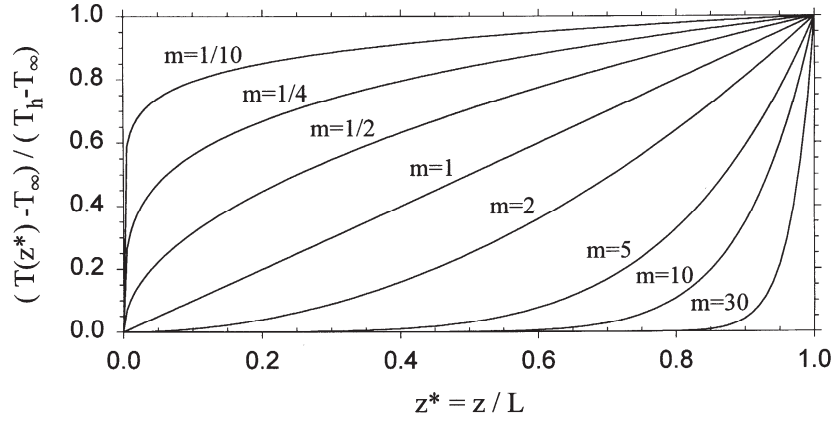


Figure 18: Dimensionless temperature profiles in the light beam direction of the form $(T(z^*) - T_\infty) / (T_h - T_\infty) = (z^*)^m$.

The difference between the arithmetic average fluid temperature (\bar{T}) and the effective fringe temperature (\bar{T}_f) can be calculated using eqns (50), (51) and (52) as follows:

$$\frac{\bar{T} - \bar{T}_f}{T_h - T_\infty} = \frac{\left(\frac{T_h - T_\infty}{m+1} + T_\infty \right) - \left[\int_0^1 \frac{1}{(T_h - T_\infty)(z^*)^m + T_\infty} dz^* \right]^{-1}}{(T_h - T_\infty)} \quad (53)$$

Eqn (53) has been evaluated for values of the exponent ranging from $0 \leq m \leq 30$. The corresponding temperature profiles are shown in Figure 18. Although these profiles do not correspond to any specific convection problem, they serve to simulate a wide range of conditions. Closed form solutions for the effective fringe temperature have been obtained for $m = 1/4, 1/2, 1, 2$ and are given in Table 3.

Figure 19 shows the effect of the overall beam temperature difference on the percentage difference between the average gas temperature and the effective fringe temperature. Data are shown for a range of exponents (m) and for $0^\circ\text{C} \leq T_h - T_\infty \leq 40^\circ\text{C}$. For interferometric measurements made in air, the overall temperature difference $T_h - T_\infty$ is usually less than 40°C in order keep refraction errors small.

It can be seen in Figure 19 that the percentage error in the fringe temperature varies linearly with the overall temperature difference along the light beam. As the temperature difference along the beam increases, the nonlinear variation of the refractive index becomes more pronounced, causing the error to increase.

Table 3: Closed form expressions for the effective fringe temperature (\bar{T}_f) for several values of the exponent m . Note that $\Delta T = T_h - T_\infty$.

Exponent m	Fringe Temp. $\bar{T}_f = \left[\int_0^1 1/(\Delta T(z^*)^m + T_\infty) dz^* \right]^{-1}$
$1/4$	$\left[\frac{4}{3\Delta T} - \frac{2T_\infty}{\Delta T^2} + \frac{4T_\infty^2}{\Delta T^3} + \frac{4T_\infty^3 \ln(T_\infty / T_h)}{\Delta T^4} \right]^{-1}$
$1/2$	$\left[\frac{2}{\Delta T} + \frac{2T_\infty \ln(T_\infty / T_h)}{\Delta T^2} \right]^{-1}$
1	$\frac{\Delta T}{\ln(T_h / T_\infty)}$
2	$\frac{\sqrt{T_\infty \Delta T}}{\tan^{-1} \sqrt{\frac{\Delta T}{T_\infty}}}$

Also, Figure 19 shows that for the general form of temperature variation considered, the effective fringe temperature is always less than the arithmetic mean temperature. However, the most striking feature of Figure 19 is the magnitude of the error. Even in the worst case, the temperature error is only slightly greater than one percent.

Figure 20 shows the variation of the percentage error in fringe temperature with the exponent (m) of the temperature variation. For all values of beam temperature difference ($T_h - T_\infty$), the maximum error occurs for an exponent of approximately $m=1.6$. At very high or very low values of the exponent (m), the error approaches zero, since the temperature is nearly uniform over most of the beam.

It also should be noted that the fringe temperature error is slightly affected by variations in the ambient temperature. The current calculations were done for $T_\infty = 300K$. As the ambient temperature increases, the error in the fringe temperature decreases slightly.

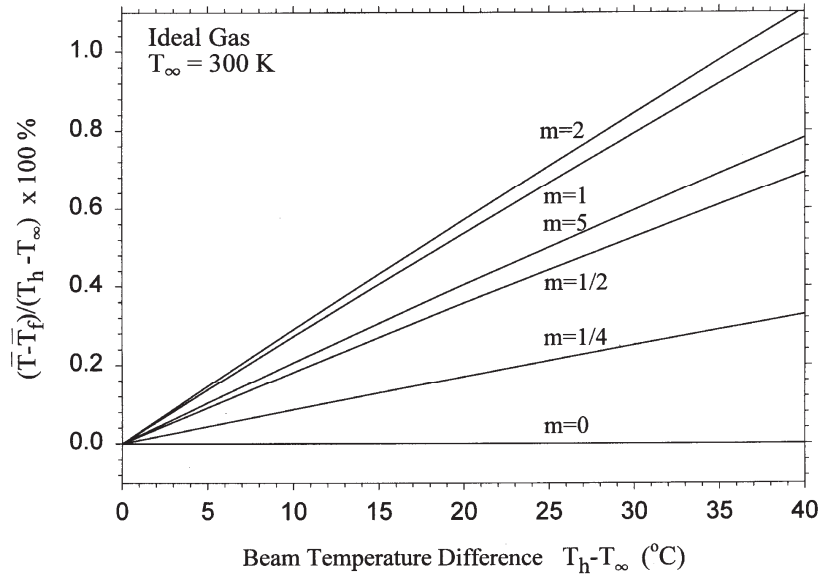


Figure 19: Effect of temperature difference on the percentage difference between the average gas temperature and the effective (i.e. measured) fringe temperature.

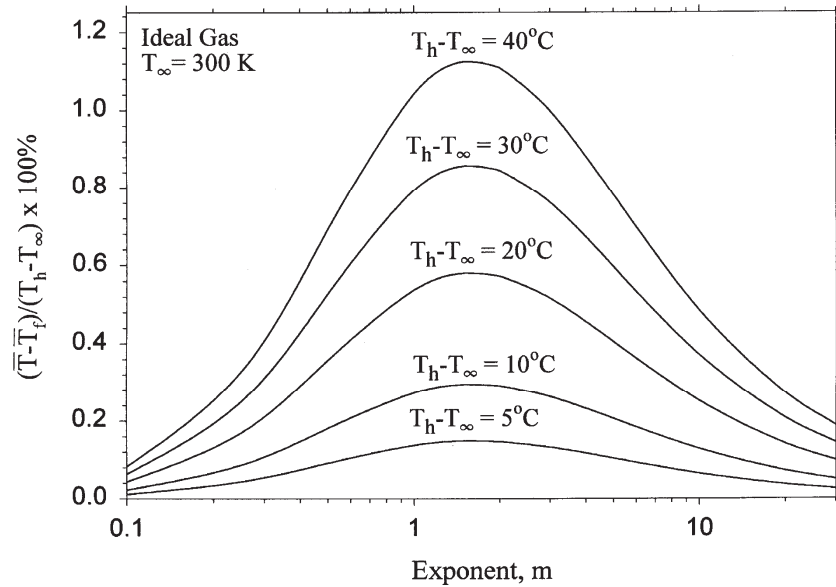


Figure 20: Effect of the temperature profile exponent on the difference between the average gas temperature and the effective (i.e. measured) fringe temperature.

The main conclusion to be drawn from this analysis is that the beam-averaged gas temperature can be closely approximation using eqn (19) as:

$$\bar{T} \approx \bar{T}_f = \frac{T_{\text{ref}}}{1 - \frac{\varepsilon(x) R \lambda_o T_{\text{ref}}}{L P G}} \quad (54)$$

For the range of conditions encountered for interferometric measurements, the error caused by this approximation usually will be small.

The above analysis was done for an ideal gas as the test fluid. Naylor and Machin [63] have repeated this analysis for water. For interferometric measurements made in water near room temperature, the fringe temperature error caused by beam-wise temperature variations was found to be less than 0.3 percent.

As shown above, the local beam-averaged heat transfer rates can be calculated from the gradient of the approximate beam-averaged temperature. Naylor [64, 65] has performed an error analysis to estimate the accuracy of such beam-averaged heat transfer measurements. The results suggest that for many commonly encountered conditions, the error will usually be small. This conclusion is also supported by interferometric measurements by Frank [59]. Frank [59] measured the free convective heat transfer from a vertical plate with large temperature variations in the beam direction.

An alternate “fringe gradient” method of calculating the beam-averaged local heat flux has been used by Papple & Tarasuk [66] for the special case of a thermally developing flow over an isothermal surface. In this method, eqn (48) is differentiated with respect to the coordinate normal to the surface (x) as follows:

$$\frac{\partial \varepsilon}{\partial x} = \frac{L P G}{R \lambda_o} \frac{\partial}{\partial x} \int_0^1 \left(\frac{1}{T_\infty} - \frac{1}{T(x, z^*)} \right) dz^* = \frac{L P G}{R \lambda_o} \int_0^1 \frac{1}{T^2} \frac{\partial T}{\partial x} dz^* \quad (55)$$

Applying eqn (55) at the surface (x=0) for an isothermal surface (T_s) gives:

$$\left. \frac{\partial \varepsilon}{\partial x} \right|_{x=0} = \frac{L P G}{R \lambda_o T_s^2} \int_0^1 \left. \frac{\partial T}{\partial x} \right|_{x=0} dz^* = \frac{L P G}{R \lambda_o T_s^2} \left. \frac{\partial \bar{T}}{\partial x} \right|_{x=0} \quad (56)$$

Solving eqn (56) for $\partial T / \partial x|_{x=0}$ and substituting the result into eqn (47) gives the local axially averaged heat transfer rate:

$$\bar{q} = -k_s \left. \frac{\partial \bar{T}}{\partial x} \right|_{x=0} = \frac{-k_s R \lambda_o T_s^2}{L P G} \left. \frac{\partial \varepsilon}{\partial x} \right|_{x=0} \quad (57)$$

In many cases, the beam-averaged local convective heat transfer coefficient (\bar{h}) is of interest and can be calculated as:

$$\bar{h} = \frac{\bar{q}}{(T_s - T_\infty)} = \frac{-k_s R \lambda_o T_s^2}{L P G (T_s - T_\infty)} \left. \frac{\partial \varepsilon}{\partial x} \right|_{x=0} \quad (58)$$

Eqn (58) can be used to calculate the axially averaged local heat transfer coefficient directly from the fringe shift gradient at the surface, which is measured (extrapolated) on the interferogram. This method is exact in the sense that it does not require the calculation of the approximate beam-averaged fluid temperature profile. For this reason, the use of eqn (57) is the preferred method for calculating the average heat transfer rate from an isothermal surface. However, for an isothermal surface, the error associated with the approximation $\bar{T}_f \approx \bar{T}$ will approach zero at the surface (see Figures 19 and 20 as $m \rightarrow 0$). So, calculation of the heat transfer rate from the gradient of the beam-averaged temperature profile can also be expected to give accurate results.

It is interesting to note that this “fringe gradient” approach is also exact for an isoflux surface. For an isoflux surface $\partial T / \partial x|_{x=0}$ is a constant. So, eqn (55) can be rearranged to give:

$$\left. \frac{\partial \bar{T}}{\partial x} \right|_{x=0} = \frac{R \lambda_o}{L P G} \left. \frac{\partial \varepsilon}{\partial x} \right|_{x=0} \left[\int_0^1 \frac{1}{T_s^2} dz^* \right]^{-1} \quad (59)$$

In applying eqn (59), the integral of the surface temperature variation could be obtained from thermocouple measurements.

5 Fringe measurement by digital image processing

The accuracy of heat transfer measurements depends to a large extent on the accuracy to which the constructive and destructive interference fringes can be located on the interferogram. In the past, interferograms were often scanned by eye using a traveling microscope or optical densitometer. In more recent times, the widespread availability of inexpensive video digitizers and image scanners, combined with the increase in computational power of computers has made routine digital image processing (DIP) of interferograms possible.

The use of DIP not only semi-automates the analysis process, but also allows image filtering operations that would not be possible using conventional optical methods. A wide range of useful image processing algorithms such as low pass filtering, binary thresholding, and contrast enhancement are now widely available in commercial photo-editing software. The reader is referred to references [67, 68, 69] for a technical discussion of DIP methods. A discussion of DIP that specifically focuses on the analysis of interferograms can be found in references [70, 71].

To illustrate its use, a simple DIP system used by Naylor and Tarasuk [72] for interferogram analysis is shown in Figure 21. In this system, a CCD video

camera was mounted onto a microscope. The camera supplied a video signal to a commercial “frame grabber” board, which was installed in a personal computer. The interferogram, recorded on a large format black and white film negative, was positioned under the microscope with a precision traveling/rotating stage. Each image was discretized into an array of 640x480 pixels, with 8 bit gray level digitization (i.e., 256 gray levels). Using this system, high spatial resolution was achieved which was limited only by the resolution of the film (approximately 160 line pairs per millimeter).

Figure 22 shows a section of an infinite fringe interferogram on the image display screen. A white line is shown on the screen to show the location of the scan, which was made perpendicular to the test model surface. Pixel intensities from a typical scan are shown in Figure 23, from which the fringe locations can be easily calculated. Vertical and horizontal scale factors can be obtained by placing a reticule under the microscope. McAulliffe and Wirtz [43] have used a similar system (without a microscope) to capture the interferogram directly from the output of the interferometer. A resolution of 0.1 mm was achieved with this “on-line” system.

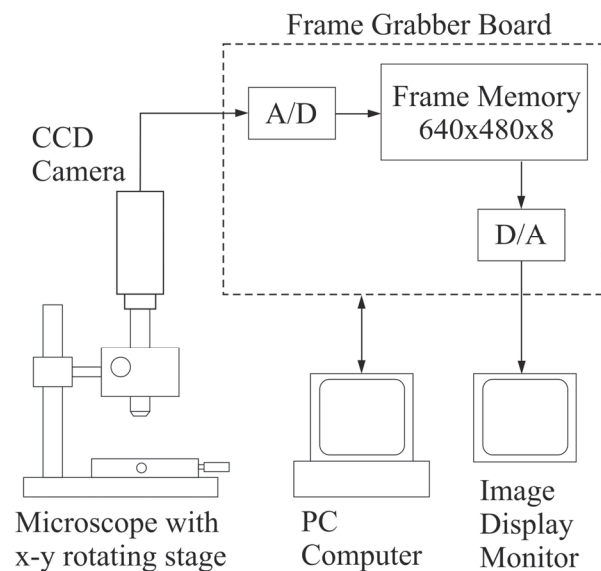


Figure 21: System for the digital image processing of interferograms [72].

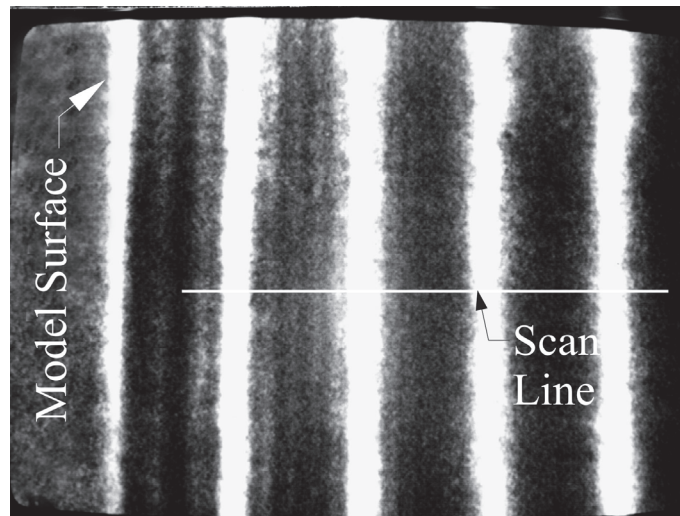


Figure 22: Display screen of the DIP system showing a horizontal scan [72].

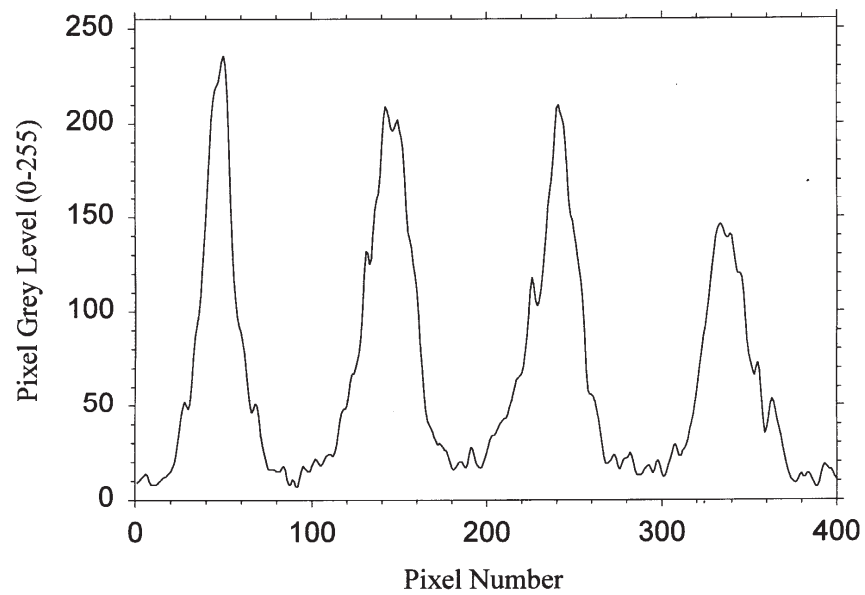


Figure 23: Variation in the pixel gray scale intensity with pixel number for the horizontal scan shown in Figure 22.

6 References

- [1] Kennard, R.B., Temperature distribution and heat flux in air by interferometry. *Temperature: Its Measurement and Control in Science and Industry*, Reinhold Publishing Corp.: New York, pp.685-706, 1939.
- [2] Eckert, E.R.G. & Soehngen, E.E., Studies on heat transfer in laminar free convection with the Mach-Zehnder interferometer. *AF Technical Report 5747*, United States Air Force, Wright Patterson Air Force Base, Dayton, Ohio, pp. 1-21, 1948.
- [3] Kwak, C.E. & Song, T.H., Natural convection around horizontal downward-facing plate with rectangular grooves: experiments and numerical simulations. *International Journal of Heat and Mass Transfer*, **43**, pp. 825-838, 2000.
- [4] Mishra, D., Muralidhar, K. & Munshi, P., Experimental study of Rayleigh-Benard convection at intermediate Rayleigh numbers using interferometric tomography. *Fluid Dynamics Research*, **25**, pp. 231-255, 1999.
- [5] Yoon, J.I., Moon, C.G., Kim, E., Son, Y.S., Kim, J.D. & Kato, T., Experimental study on freezing of water with supercooled region in a horizontal cylinder. *Applied Thermal Engineering*, **21**, pp. 657-668, 2001.
- [6] Herman, C. & Kang, E., Comparative evaluation of three heat transfer enhancement strategies in a grooved channel. *Heat and Mass Transfer*, **37**, pp. 563-575, 2001.
- [7] Liou, Y.-M., Some applications of experimental and numerical visualization in fluid flow, heat transfer and combustion. *Experimental Thermal and Fluid Science*, **25**, pp. 359-375, 2001.
- [8] Lockett, J.F. & Collins, M.W., Problems in using holographic interferometry to resolve the four-dimensional character of turbulence. Part I: Theory and Experiment. *Journal of Optical Sensors*, **1(3)**, pp. 211-224, 1986.
- [9] Hunter J. & Collins, M.W., Problems in using holographic interferometry to resolve the four-dimensional character of turbulence. Part II: Image and data processing. *Journal of Optical Sensors*, **1(3)**, pp. 277-234, 1986.
- [10] Kuehn, T.H., Natural convection heat transfer from a horizontal cylinder to a surrounding cylindrical enclosure. *Ph.D. Thesis*, University of Minnesota, 1976.
- [11] Kuehn, T.H. & Goldstein, R.J., An experimental study of natural convection heat transfer in concentric and eccentric horizontal annuli. *Journal of Heat Transfer*, **100**, pp. 635-640, 1978.
- [12] Goldstein, R.J., Optical measurement of temperature. *Measurement Techniques in Heat Transfer*, eds. E.R.G. Eckert and R.J. Goldstein, Technivision Services, Slough, England, pp. 177-228, 1970.
- [13] Hauf, W. & Grigull, U., Optical methods in heat transfer. *Advances in Heat Transfer*, eds. J.P. Harnett & T.F. Irvine, Jr., Academic Press: New York, vol. 6, pp. 133-366, 1970.
- [14] Goldstein, R.J., Interferometer for aerodynamic and heat transfer measurements. *The Review of Scientific Instruments*, **36 (10)**, pp. 1408-1410, 1965.

- [15] Tanner, L.H., The design of laser interferometers for use in fluid mechanics. *Journal of Scientific Instruments*, **43**, pp. 878-886, 1966.
- [16] Papple, M.C.L. & Tarasuk, J.D., Natural convection about vertical cylinders immersed in a variable property gas. *ASME/AICHE National Heat Transfer Conference*, paper 85-HT-15, pp. 1-8, 1985.
- [17] Fröhlich, T., Guenoun, P., Bonetti, M., Perrot, F., Beysens, D., Garrabos, Y., Le Neindre, B. & Bravais, P., Adiabatic versus conductive heat transfer in off-critical SF₆ in the absence of convection. *Physical Review E*, **54**(2), pp. 1544-1549, 1996.
- [18] Papple, M.L.C., Laminar natural convection about vertical cylinders including variable fluid properties. *M.E.Sc. Thesis*, The University of Western Ontario, London, Ontario, 1984.
- [19] Yan, D. & Cha, S.S., Practical common-path interferometry for real-time thermal/fluid flow measurements. *Int. Comm. Heat Mass Transfer*, **25**(1), pp.1-8, 1998.
- [20] Sheng-jie, X., Double mirror laser interferometer. *Proc. 3rd Int. Conference on Flow Visualization*, Ann Arbor, Michigan, U.S.A., pp. 155-159, 1983.
- [21] Vest, C.M., *Holographic Interferometry*, John Wiley & Sons: New York, 1979.
- [22] Mayinger, F. (ed.), *Optical Methods - Techniques and Applications*, Springer-Verlag: New York, 1994.
- [23] Kreis, T., *Holographic Interferometry - Principles and Methods*, Akademie Verlag: Berlin, 1996.
- [24] Hariharan, P., Basic principles (Chapter 2), *Holographic Interferometry - Principles and Methods*, ed. P.K. Rastogi, Springer-Verlag: Berlin, pp. 7-32, 1994.
- [25] Ostrovsky, Y.I., Butusov, M.M. & Ostrovskaya, G.V., *Interferometry by Holography*, Springer-Verlag: New York, 1980.
- [26] Gabor, D., A new microscopic principle. *Nature*, **161**, pp. 777-778, 1948.
- [27] Gabor, D. Microscopy by reconstructed wavefronts. *Proc. Royal Society A*, **197**, pp. 454-487, 1949.
- [28] Gabor, D., Microscopy by reconstructed wavefronts: II. *Proc. Royal Society B*, **64**, pp. 449-469, 1951.
- [29] Zinnes, A.E., The coupling of conduction with laminar natural convection from a vertical flat plate with arbitrary surface heating. *Journal of Heat Transfer*, **92**, Series C, pp. 528-535, 1970.
- [30] Cesini, G., Paroncini, M., Cortella, G. & Manzan, M., Natural convection from a horizontal cylinder in a rectangular cavity. *International Journal of Heat and Mass Transfer*, **42**, pp. 1801-1811, 1999.
- [31] Cha, D.J. & Cha, S.S., Three-dimensional natural convection flow around two interacting isothermal cubes. *International Journal of Heat Mass Transfer*, **38** (13), pp. 2343-2352, 1995.
- [32] Fehle, R., Klas, J. & Mayinger, F., Investigation of local heat transfer in compact heat exchangers by holographic interferometry. *Experimental Thermal and Fluid Science*, **10**, pp. 181-191, 1995.

- [33] Kilicaslan, I., & Sarac, H.I., Enhancement of heat transfer in compact heat exchanger by different type of rib with holographic interferometry. *Experimental Thermal and Fluids Science*, **17(4)**, pp. 339-346, 1998.
- [34] Liou, T.-M. & Wang, W.-B., Laser holographic study of developing heat transfer in a duct with a detached rib array. *International Journal of Heat & Mass Transfer*, **38 (1)**, pp. 91-100, 1995.
- [35] Kato, S., Maruyama, N. & Tabejamatt, S., Numerical simulation and laser holographic study of thermal diffusion in counterflow with different temperatures. *Energy Conversion and Management*, **38 (10-13)** , pp. 1197-1207, 1997.
- [36] Mayinger, F., Fundamentals of holography and interferometry (Chapter 4), *Optical Methods - Techniques and Applications*, ed. F. Mayinger, Springer-Verlag: New York, pp. 27-50, 1994.
- [37] Born, M. & Wolf, E., *Principles of Optics*, Pergamon Press: Oxford, 1980.
- [38] Merzkirch, W., *Flow Visualization*, Academic Press Inc.: New York, 1987.
- [39] Tilton, L.W. & Taylor, J.K., Refractive index and dispersion of distilled water for visible radiation, at temperatures 0 to 60°C. *Journal of Research of the National Bureau of Standards*, **20**, pp. 419-477, 1938.
- [40] Dobbins, H.M. & Peck, E.R., Change in refractive index of water as a function of temperature. *Journal of the Optical Society of America*, **63 (3)**, pp. 318-320, 1973.
- [41] Murphy, C.G. & Alpert, S.S., Dependence of refractive index temperature coefficient on the thermal expansivity of liquids. *Am. J. Phys.*, **39**, pp. 834-836, 1971.
- [42] Khuen, T.H. & Goldstein, R.J., An experimental and theoretical study of natural convection in the annulus between horizontal concentric cylinders. *Journal of Fluid Mechanics*, **100(4)**, pp. 695-719, 1976.
- [43] McAuliffe, W. & Wirtz, R.A., Application of on-line image analysis to local convective heat transfer measurements. *Fundamental Experimental Measurements in Heat Transfer*, ASME HTD-vol. 179, pp. 1-5, 1991.
- [44] Breuckmann, B. & Thieme, W., Computer-aided analysis of holographic interferograms using the phase-shift method. *Applied Optics*, **24**, pp. 2145-2149, 1985.
- [45] Slepicka, J.S. & Cha, S.S., Stabilized nonlinear regression for interferogram analysis. *Applied Optics*, **34**, pp. 5039-5044, 1995.
- [46] Duarte, N., Naylor, D., Oosthuizen, P.H. & Harrison, S.J., An interferometric study of free convection at a window glazing with a heated Venetian blind. *International Journal of HVAC&R Research*, **7(2)**, pp. 169-184, 2001.
- [47] Naylor, D. & Duarte, N., Direct temperature gradient measurement using interferometry. *Experimental Heat Transfer*, **12(4)**, pp. 279-294, 1999.
- [48] Lacona, E. & Taine, J., Holographic interferometry applied to coupled free convection and radiative heat transfer in a cavity containing a vertical plate between 290 and 650 K, *International Journal of Heat and Mass Transfer*, **44**, pp. 3755-3764, 2001.
- [49] Dietz, G. & Balkowski, I., Interferometry and reconstruction of strongly refracting fields in two-dimensional boundary layer flow. *Experiments in Fluids*, **12**, pp. 423-431, 1997.

- [50] Mehta, J.M. & Black, W.Z., Errors associated with interferometric measurement of convective heat transfer coefficients. *Applied Optics*, **16(6)**, pp. 1720-1726, 1977.
- [51] Flack, R.D., Mach-Zehnder interferometer errors resulting from test section misalignment. *Applied Optics*, **17 (7)**, pp. 985-987, 1978.
- [52] Bahl, S. & Liburdy, J.A., Measurement of local convective heat transfer coefficients using three-dimensional interferometry. *International Journal of Heat and Mass Transfer*, **34 (4-5)**, pp. 949-960, 1991.
- [53] Sweeney, D.W. & Vest, C.M., Measurements of three-dimensional temperature fields above heated surfaces by holographic interferometry. *International Journal of Heat and Mass Transfer*, **17**, pp. 1443-1454, 1974.
- [54] Cha, S.S. & Sun, H., Tomography for reconstructing continuous fields from ill-posed multidirectional interferometric data. *Applied Optics*, **29 (2)**, pp. 251-258, 1990.
- [55] Cha, D.J. & Cha, S.S., Holographic interferometric tomography for limited data reconstruction. *AIAA Journal*, **34 (5)**, pp. 1019-1026, 1996.
- [56] Sweeney, D.W., A comparison of Abel integral equation inversion schemes for interferometric applications. *J. Opt. Soc. Am.*, **64**, p. 559, 1974.
- [57] Lai, B.Y. & Naylor, D., Measurement of the spanwise free convective heat transfer distribution on an inclined upward-facing heated plate. *12th Int. Heat Transfer Conference*, Grenoble, France, vol. 2, pp. 645-650, 2002.
- [58] Papple, M.L.C., Developing laminar natural convective flow in inclined square ducts: A preliminary study. *Ph.D. Thesis*, The University of Western Ontario, London, Ontario, 1988.
- [59] Frank, M.E., Interferometer measurements in free convection on a vertical plate with temperature variation in the light-beam direction. *Fourth International Heat Transfer Conf.*, eds. U. Grigull & E. Hahne, Elsevier: Amsterdam, vol. 4, pp. 1-12, 1970.
- [60] Frank, M.E., Effect of vortices induced by corona discharge on free-convection heat transfer from a vertical plate. *Trans. ASME*, **91 (3)**, Series C, pp. 427-433, 1969.
- [61] McKeen, W.J., An interferometric study of combined forced and free convective heat transfer in the entrance region of horizontal concentric annuli. *Ph.D. Thesis*, The University of Western Ontario, London, Ontario, 1981.
- [62] Yousef, W.W. & Tarasuk, J.D., An interferometric study of combined free and forced convection in a horizontal isothermal tube. *Journal of Heat Transfer*, **103**, pp. 249-256, 1981.
- [63] Naylor, D. & Machin, A.D., The accuracy of beam-averaged interferometric temperature measurements in a three-dimensional field. *Experimental Heat Transfer*, **14(3)**, pp. 217-228, 2001.
- [64] Naylor, D., On the accuracy of beam-averaged interferometric heat transfer measurements. *Journal of Heat Transfer*, **24(5)**, pp. 1072-1077, 2002.
- [65] Naylor, D., An error analysis of beam-averaged interferometric heat transfer measurements. *International Mechanical Engineering Congress and Exposition*, ASME Paper HTD-24409, pp. 1-8, 2001.
- [66] Papple, M.L.C., & Tarasuk, J.D., An interferometric study of developing

- natural convective flow in inclined isothermal ducts. *AIAA 22nd Thermophysics Conference*, Hawaii, Paper 87-1589, pp. 1-8, 1987.
- [67] Gonzalez, R.C. & Woods, R.E., *Digital Image Processing*, Addison-Wesley: Reading, Mass., 1992.
- [68] Russ, J.C., *The Image Processing Handbook*, Second edition, CRC Press: Boca Raton, Florida, 1995.
- [69] Baxes, G.A., *Digital Image Processing: A Practical Primer*, Prentice-Hall: Englewood Cliffs, New Jersey, 1984.
- [70] Nübel, R., Computer-aided evaluation method for interferograms. *Experiments in Fluids*, **12**, pp. 166-172, 1992.
- [71] Robinson, D.W. & Reid, G.T., (eds). *Interferogram Analysis: Digital Fringe Pattern Measurement Techniques*, Institute of Physics Publishing: Bristol, England, 1993.
- [72] Naylor, D. & Tarasuk, J.D., Digital image processing of interferograms for local convective heat transfer measurements. *Proc. of the 3rd World Conf. on Experimental Heat Transfer, Fluid Mechanics and Thermodynamics*, eds. M.D. Kelleher et al., Elsevier: Amsterdam, vol. 2, pp. 1609-1614, 1993.
- [73] Naylor, D. Recent developments in the measurement of convective heat transfer rates by laser interferometry. *Int. J. Heat and Fluid Flow*, **24**, pp. 345-355, 2003.

7 Nomenclature

A	light wave amplitude
c	speed of light (m/s)
c ₀	speed of light in a vacuum (m/s)
C	constant in eqn (34) (W/m ² K)
d	finite (wedge) fringe spacing (m)
d _{opt}	optimum finite fringe spacing (m)
DIP	digital image processing
G	Gladstone-Dale constant (m ³ /kg)
h	local convective heat transfer coefficient (W/m ² K)
\bar{h}	axially averaged local convective heat transfer coefficient (W/m ² K)
k	fluid thermal conductivity (W/mK)
k _s	fluid thermal conductivity at the surface temperature (W/mK)
L	length of test model in beam direction (m)
m	exponent of the temperature variation along the light beam
MZI	Mach-Zehnder interferometer
n	fluid refractive index
n _∞	fluid refractive index at the ambient conditions
n _{ref}	refractive index at reference conditions
P	absolute fluid pressure (Pa)
q	local heat flux (W/m ²)
\bar{q}	axially averaged local heat flux (W/m ²)
r	radial coordinate (m)

\bar{r}	specific refractivity (m^3/kg)
R	gas constant (J/kgK)
S	optical path length (m)
t	time (s)
T	absolute temperature (K)
\bar{T}	true axially averaged fluid temperature (K)
\bar{T}_f	effective fringe (i.e. measured) temperature (K)
T_h	fluid temperature at the exit of the test section (K)
T_{ref}	reference temperature (K)
T_s	surface temperature (K)
T_∞	ambient temperature (K)
w	distance on wedge fringe interferogram (m)
x, y	Cartesian coordinates (m)
z	coordinate in the direction of the object/test beam (m)
z^*	dimensionless coordinate, z/L

Greek Symbols

α	wedge fringe angle at the solid/fluid interface (rad)
β	fluid volume expansion coefficient (K^{-1})
γ	finite (wedge) fringe angle at ambient conditions (rad)
δ	thermal boundary layer thickness (m)
$\Delta\epsilon_r$	fringe shift caused by refraction
ΔT	temperature difference along a light ray (K)
ϵ	fringe shift order
θ	reference and test beam recombination angle (rad)
λ	wavelength of light (m)
λ_o	vacuum wavelength of light (m)
ρ	fluid density (kg/m^3)
ϕ	phase shift (rad)

Subscripts

ref	reference beam
s	solid/fluid interface ($x=0$)
∞	ambient conditions

8 Acknowledgments

The author gratefully acknowledges the assistance of the staff of Ryerson University Library. The author also wishes to thank Kathryn Naylor and Alan D. Machin for their assistance with the preparation of this chapter.